

AD-A109 725

SYSTEMS SCIENCE AND SOFTWARE LA JOLLA CA
ANALYSIS OF JETTING SIMULATION EXPERIMENTS. (U)
JUL 81 J R BARTHEL, J W WIEHE

F/G 18/3

DNA001-81-C-0072

UNCLASSIFIED

SSS-R-81-4898

DNA-TR-81-30

NL

[illegible]

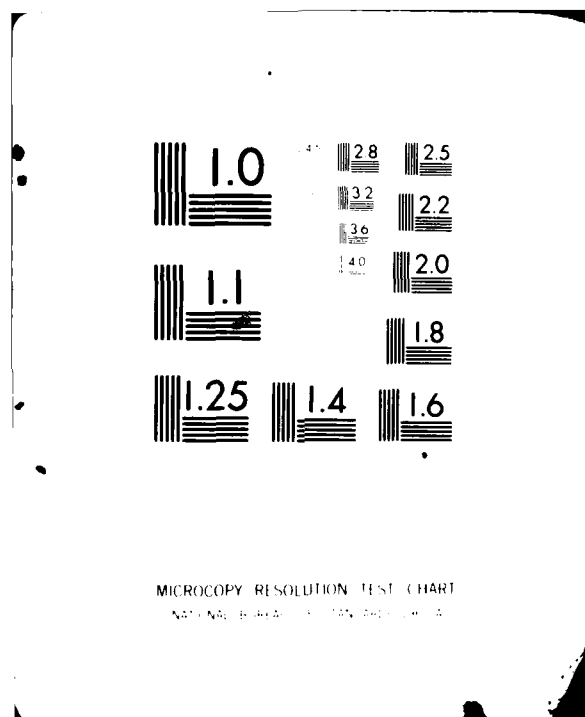
END

DATE _____

FILMED

100

NTIC



AD A109725

12

DNA-TR-81-30

ANALYSIS OF JETTING SIMULATION EXPERIMENTS

J. R. Barthel
J. W. Wiehe
Systems, Science and Software, Inc.
P.O. Box 1620
La Jolla, California 92037

1 July 1981

Technical Report

CONTRACT No. DNA 001-81-C-0072

APPROVED FOR PUBLIC RELEASE;
DISTRIBUTION UNLIMITED.

DTIC FILE COPY

THIS WORK SPONSORED BY THE DEFENSE NUCLEAR AGENCY
UNDER RDT&E RMSS CODES B345081466 J24AAXYX00010 H2590D
AND B345081466 J24AAXYX00011 H2590D.

Prepared for
Director
DEFENSE NUCLEAR AGENCY
Washington, D. C. 20305

01 18 82 39

Destroy this report when it is no longer
needed. Do not return to sender.

PLEASE NOTIFY THE DEFENSE NUCLEAR AGENCY,
ATTN: STTI, WASHINGTON, D.C. 20305, IF
YOUR ADDRESS IS INCORRECT, IF YOU WISH TO
BE DELETED FROM THE DISTRIBUTION LIST, OR
IF THE ADDRESSEE IS NO LONGER EMPLOYED BY
YOUR ORGANIZATION.



UNCLASSIFIED

SECURITY CLASSIFICATION OF THIS PAGE (When Data Entered)

REPORT DOCUMENTATION PAGE		READ INSTRUCTIONS BEFORE COMPLETING FORM
1. REPORT NUMBER DNA-TR-81-30	2. GOVT ACCESSION NO. ADA109725	3. RECIPIENT'S CATALOG NUMBER
4. TITLE (and Subtitle) ANALYSIS OF JETTING SIMULATION EXPERIMENTS		5. TYPE OF REPORT & PERIOD COVERED Technical Report
		6. PERFORMING ORG. REPORT NUMBER SSS-R-81-4898
7. AUTHOR(s) J. R. Barthel J. W. Wiehe		8. CONTRACT OR GRANT NUMBER(s) DNA 001-81-C-0072
9. PERFORMING ORGANIZATION NAME AND ADDRESS Systems, Science and Software, Inc. P.O. Box 1620 La Jolla, California 92037		10. PROGRAM ELEMENT, PROJECT, TASK AREA & WORK UNIT NUMBERS Subtasks J24AAXYX 000-10 J24AAXYX 000-11
11. CONTROLLING OFFICE NAME AND ADDRESS Director Defense Nuclear Agency Washington, D. C. 20305		12. REPORT DATE 1 July 1981
		13. NUMBER OF PAGES 74
14. MONITORING AGENCY NAME & ADDRESS (if different from Controlling Office)		15. SECURITY CLASS. (of this report) UNCLASSIFIED
		15a. DECLASSIFICATION/DOWNGRADING SCHEDULE
16. DISTRIBUTION STATEMENT (of this Report) Approved for public release; distribution unlimited.		
17. DISTRIBUTION STATEMENT (of the abstract entered in Block 20, if different from Report) This work sponsored by the Defense Nuclear Agency under RDT&E RMSS Codes B345081466 J24AAXYX00010 H2590D and B345081466 J24AAXYX00011 H2590D.		
18. SUPPLEMENTARY NOTES		
19. KEY WORDS (Continue on reverse side if necessary and identify by block number) LOS Flow Simulation Vapor Flow Particulate Jetting Cratering		
20. ABSTRACT (Continue on reverse side if necessary and identify by block number) This report describes calculational and analytical studies of high explosive jetting experiments designed to simulate energy injection into a nuclear line of sight. Numerous experiments were performed (by Physics International Co.) using identical spherical HE sources embedded in wet sand. Damage was assessed by comparing the volume and depth of holes produced in aluminum target plates at the end of each pipe. An evacuated steel pipe, 19 mm o.d. and 0.3 mm thick, was the standard configuration. Many variations were used. (continued)		

DD FORM 1473 EDITION OF 1 NOV 65 IS OBSOLETE

UNCLASSIFIED

SECURITY CLASSIFICATION OF THIS PAGE (When Data Entered)

UNCLASSIFIED

SECURITY CLASSIFICATION OF THIS PAGE(When Data Entered)

Axially symmetric experiments produced some unexpected results, for example: use of a 2 mm jacket of lead around a standard pipe produced holes about twice as great in depth and volume as the average of the standard configurations; use of an air-filled pipe with wall thickness of 0.7 mm produced triple the standard hole size. Two-dimensional calculations for the Standard and Lead Wrap cases which did not include the thin pipe wall were totally inconsistent with these results. Calculations including the wall were quite consistent with the data if relative energy in the particulate jet of wall material formed on collapse is compared with measured hole volume. In terms of absolute comparisons, the calculated results are consistent only if the cratering efficiency of the shower of particulate matter is assumed to be three to five times smaller than that of a single particle at the same velocity - which is considered reasonable.

Simplified calculation including the wall were performed for all three axisymmetric configurations in the frame of reference of a steady shock to provide guidance for the calculations of the actual configurations with a decaying shock. These produced the unexpected result that all three jet particulate mass and energy at equal rates as a steady state is approached. This result is explained by an adaptation of impulsive jetting theory. The steady state results put constraints on explanations of the laboratory results. The stronger jetting in the Lead Wrap case, compared with the Standard, is attributed to slower response of the region of the source of the jet to decay in the driving pressure in the wet sand - the Lead Wrap configuration is better tamped. The 0.7 mm air filled pipe result is explained analogously.

➤ Configurations employing helical spiral asymmetries, 0.3 to 0.5 mm thick, also produced unexpected results. Spirals resting against the outer pipe wall resulted in essentially no change in target damage, whereas spirals resting against the inner wall virtually eliminated target damage. As a consequence, original intuition that the spiral would prevent cratering because of inertial effects was abandoned. A postulated mechanism attributing the spiral effect to turning of the unattached spiral into the pipe by the action of the faster-arriving vapor flow (generated by energetic pipe implosion near the source) is presented in detail. This mechanism is shown to be consistent with all data acquired so far in the series of experiments.

UNCLASSIFIED

TABLE OF CONTENTS

<u>Section</u>	<u>Page</u>
LIST OF ILLUSTRATIONS- - - - -	2
LIST OF TABLES - - - - -	4
1 INTRODUCTION - - - - -	5
2 SYMMETRIC CONFIGURATIONS - - - - -	10
3 ASYMMETRIC CONFIGURATIONS - - - - -	25
4 IMPLICATIONS FOR UNDERGROUND NUCLEAR TESTING - - - - -	28
5 CONCLUSIONS AND RECOMMENDATIONS - - - - -	31
REFERENCES - - - - -	33
APPENDIX	
A CALCULATIONS OF JETTING WITH A STEADY SHOCK - - - - -	35
B AERODYNAMIC TWISTING OF THE HELICAL SPIRAL - - - - -	-63

Approved For	
By	
Date	
Initials	
Signature	
Distribution	
MAIL ROOM	
Dist	Special
A	

LIST OF ILLUSTRATIONS

<u>Figure</u>		<u>Page</u>
1.1	Configuration of the LS-II Experiment- - - - -	6
2.1	STREAK initial configuration showing zoning and package boundary- - - - -	13
2.2	Evolution of the pipe collapse and particulate jet in the calculation of the PI Standard configuration- - - - -	15
2.3	Evolution of the pipe collapse and particulate jet in the calculation of the PI Lead Wrap configuration	16
2.4	Growth of kinetic energy in the particulate jet - - - -	18
2.5	Growth of total energy in the vapor ahead of the collapse point- - - - -	19
2.6	Arrival and penetration data from Standard and Polyolefin spiral configurations of LS III - - - - -	20
APPENDIX		
A.1	Initial configuration for calculations in steady shock frame of reference - - - - -	36
A.2	Condensate mass flux out of the computational grid - - -	38
A.3	Vapor mass flux out of the computational grid - - - -	39
A.4	Flux of condensate kinetic energy out of the computational grid- - - - -	41
A.5	Flux of total vapor energy out of the computational grid - - - - -	42
A.6	Impulsive jetting configuration considered in simplified theory - - - - -	43
A.7	Steady shock-driven jetting configuration- - - - -	45
A.8	Tracer positions in idealized Standard configuration, 25 μ s- - - - -	49
A.9	Pressure contours in idealized Standard configuration, 25 μ s- - - - -	50
A.10	Density contours in idealized Standard configuration, 25 μ s- - - - -	51

LIST OF ILLUSTRATIONS

<u>Figure</u>		<u>Page</u>
A.11	Velocity vectors in idealized Standard configuration, 25 μ s- - - - -	52
A.12	Tracer positions in idealized Lead Wrap configuration, 25 μ s- - - - -	53
A.13	Pressure contours in idealized Lead Wrap configuration, 25 μ s- - - - -	54
A.14	Density contours in idealized Lead Wrap configuration, 25 μ s- - - - -	55
A.15	Velocity vectors in idealized Lead Wrap configuration, 25 μ s- - - - -	56
A.16	Tracer positions in idealized Pinex configuration, 25 μ s- - - - -	57
A.17	Pressure contours in idealized Pinex configuration, 25 μ s- - - - -	58
A.18	Density contours in idealized Pinex configuration, 25 μ s- - - - -	59
A.19	Velocity vectors in idealized Pinex configuration, 25 μ s- - - - -	60
B-1	Geometry of twisting spiral- - - - -	64
B-2	Resistance of the helical sheet to twisting - - - - -	69

LIST OF TABLES

<u>Table</u>		<u>Page</u>
1.1	Summary of results of Physics International simulation experiments, LS II, III, IV - - - - -	7
2.1	Hole volume statistics for symmetric configurations - -	11
APPENDIX		
A.1	Comparison of collapse angles, θ° , implied by simplified theory and measured from calculation output - - - - -	48
A.2	Comparison of jetting energy rate inferred from \dot{M}_j and calculated directly- - - - -	48

SECTION 1

INTRODUCTION

A series of high explosive-driven laboratory experiments has been carried out by Physics International Co., (PI) over the past several years to simulate energy injection into a nuclear line-of-sight pipe (LOS). The purpose was to gain better understanding of the mechanism of energy injection into the LOS and to test means of minimizing this energy through the use of various symmetric and asymmetric configurations.

The experiments considered in this report are known as LS II, III, and IV. These each employed a spherical charge of nitromethane embedded in a large container of saturated sand. This drove a spherically divergent shock in the sand as in an underground nuclear test. A number of pipe configurations extending in various directions from the sphere were employed on each test (nearly all were evacuated). The shock-driven collapse of these pipes caused energetic jetting. Aluminum witness plates at the end of each pipe were used to assess the jetting. Figure 1.1 shows the arrangement of LS II; LS III, IV were similar. Greater detail is available in Ref. 1.

The detailed findings of these experiments are described in Refs. 1 and 2. Ref 3 also includes an adequate presentation of LS II, III results. Table 1.1 contains a brief description of all pipe configurations tested in the series and the penetration depth and hole volume in the witness plate for each. The major findings of the LS series may be summarized as follows:

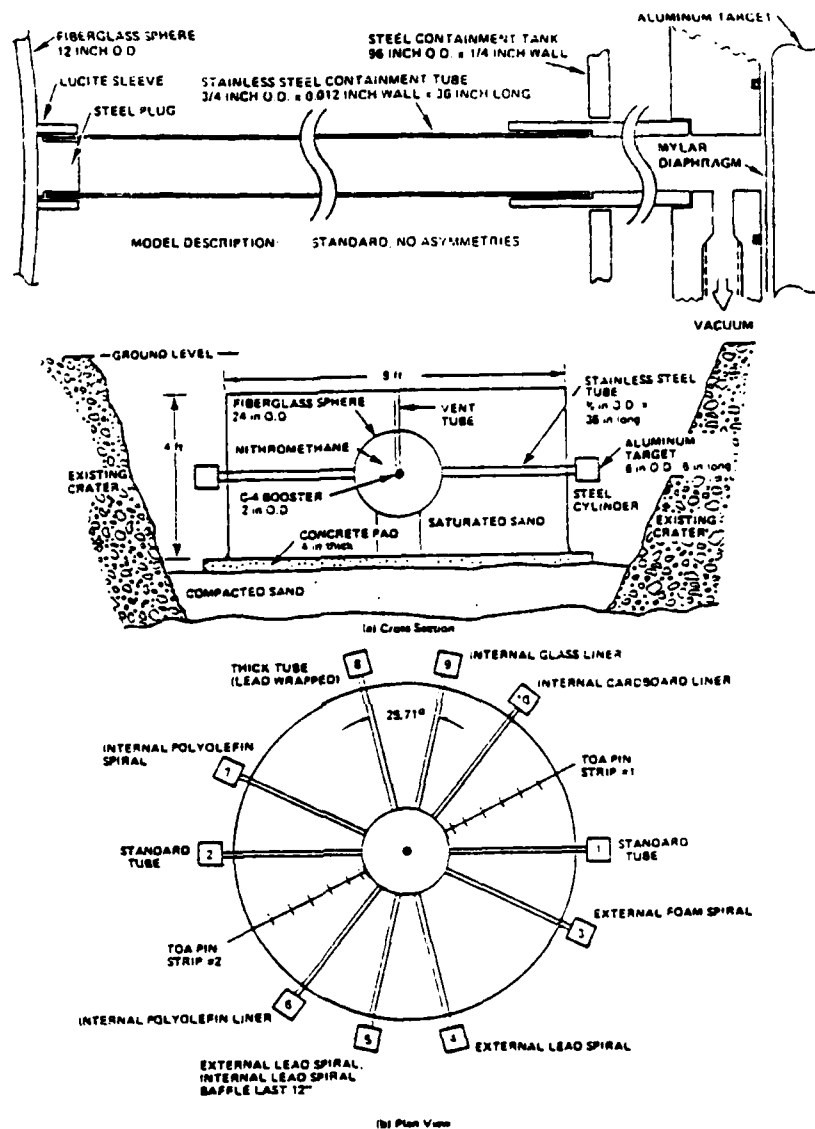


Figure 1.1 Configuration of the LS-II Experiment. [LS-III, IV were similar to this. Standard Model shown; Other Models are variants of this. This Figure is taken from Reference 1]

TABLE 1.1
SUMMARY OF RESULTS OF PHYSICS INTERNATIONAL SIMULATION EXPERIMENTS
LS II, III, IV
Lengths: II > .914 m
III, IV > .994 m

SYMMETRIC*

ASYMMETRIC (†)

Configuration	No.	Description	Hole Vol (cc)	Depth (cm)	Configuration	No.	Description	Hole Vol (cc)	Depth (cm)
Standard	II-1 2 III-1 10 11 14 IV-1 2	19.05 mm o.d., 0.30 mm thk	16.5	5.75 3.4 4.4 13.0 25.0 33.0 22.0 14.8 8.8	External Spiral Wrap	II-4 II-5 II-3	Pb 2.03 mm thk same + internal spiral last 305 mm, 3.18 mm thk Foam 2.54 mm thk	17.0 0 13.6	4.2 0 4.15
Pine	III-20 IV-17	1 atm, .71 mm thk pipe 1 atm, .30 mm thk pipe	61.5 25.5	14.9 6.5	Internal Spiral Asym	III-7 III-7 III-8 III-17 III-19 III-15 III-16 III-5 III-6 IV-3 IV-4 IV-19 IV-21 IV-22 IV-22E IV-8 IV-9	Polyolefin .36 mm thk Polyolefin .41 mm thk Same + 1 atm (this only) Spiral 1st 152 mm Spiral 1st 229 mm Pb .33 mm thk Steel .46 mm thk Steel .51 mm thk 1 atm HE Intrusion 1st 300 mm only Jet (pipe 216 mm into HE) .51 mm thk, (last 384 mm only)	0 0 0 0 0 12.2 2.8 0** 0 0 0 0 0 0 7.6 0 0 0	0 0 0 0 0 3.9 1.2 0 0 0 0 0 0 5.0 0 0 0
Glass Liner	II-9	1 liner .51 mm	31.5	7.7					
Cardboard liner	II-10	1 liner .46 mm	10.6	5.8					
Polyolefin liner	II-6	1 liner .36 mm	17.2	7.2					
Heavy Pb Wrap	II-8 IV-5 IV-7	2.03 mm thk " "	37.2 31.5 50.0	9.2 9.0 13.5					
Standoff	III-2 III-3 III-4 IV-20E	102 mm sand 203 mm sand 305 mm sand 500 mm sand	15.5 11.5 8.4 3.4	5.3 4.9 2.7 1.2	Spiral baffle	III-12	Pb spiral, 3.18 x 3.18 mm last 384 mm	0**	0
HE Intrusion	IV-20	HE first 38 mm of pipe	15.5	7.0	Ring baffle	IV-10 IV-11	Pb, 3.18 x 3.18 mm last 384 mm only	0 0	0 0
Jet	IV-2E	(pipe 216 mm into HE)	46.5	12.6	Muffler last 384 mm only	IV-13 IV-14 IV-15 IV-16	Pb rings 3.18 x 3.18 mm Same Pb spirals 3.18 x 3.18 mm Same	6.4 7.5 5.8 14.6	2.5 3.8 3.8 6.5
					Linear Asym	III-13	Straight .41 mm Polyolefin strip	11.4	6.3

* All use steel pipe; all pipes except III-20 are same as Standard.

† Spiral unless otherwise noted

** = relatively smooth

+ = order 1mm

Other zeros imply pitted surface

- The Standard symmetric configuration was employed eight times in all. A relatively wide variation in target damage was observed.
- Use of an external spiral asymmetry or an internal axial strip asymmetry produced no qualitative reduction in damage to the target.
- Use of an internal spiral asymmetry drastically reduced the damage to the target for all spiral materials used (polyolefin, steel, lead).
- The damage reduction remained dramatic for spiral asymmetries (or for spiral or ring baffles inside the pipe) occupying only the last 38 cm of the approximately 1 m total pipe length but was only moderate for spiral asymmetries occupying the first 30 cm or less.
- Mufflers occupying the last 38 cm of pipe length reduced the average damage only moderately, whether the baffles employed were spirals or symmetric rings (these baffles did not intrude into the pipe).
- Use of a heavy symmetric Lead Wrap with the Standard configurations increased the average damage significantly - considerable variation in damage was again observed in duplicate experiments.
- The greatest damage level of all was attained with an air-filled pipe with walls 2.3 times as thick as the Standard pipe. This is attributed to the pipe thickness - a repeat of the Standard with air produced results similar to the average of the Standard cases.

- Air at 1 atm apparently had no effect on the performance of any of the symmetric or asymmetric configurations on which it was used.
- "Standoff" experiments using regions of wet sand of varying length between the spherical source and the beginning of the pipe indicate that most of the jetting energy is injected in the first 25 cm of pipe length and nearly all of it in the first 50 cm.

The calculational and analytical effort by S Cubed on this program has two principal objectives: first, to determine how well calculations match the axially symmetric results and make any necessary improvements; and second, to provide scenarios to explain both the symmetric and the asymmetric observed phenomena. The initial effort on this program, which was only partially successful, is described in Ref. 3. The effort described here tentatively fulfills the program objectives, subject to the findings of the forthcoming LS V experiment which is designed in part to clarify the proposed scenarios. Nevertheless, some further calculations would be desirable as time and resources permit.

The calculations and analyses of the symmetric configurations are discussed in Section 2. A scenario for the performance of the asymmetric configurations, clarifying, with the guidance of LS IV data, issues that were left unresolved in Ref. 3, is presented in Section 3. The implications of the results for underground nuclear testing are discussed in Section 4. A summary of conclusions and recommendations is given in Section 5.

SECTION 2

SYMMETRIC CONFIGURATIONS

The symmetric configurations used in the experiments produced some unexpected results which have not been previously explained. This section is concerned with those, in particular, the comparisons between the Standard configuration, the configuration with a heavy Lead Wrap, and the "Pinex" configuration - which contained air in the pipe at 1 atm (the others were evacuated). Results which were already understood in terms of the calculational analysis in Ref. 3, e.g., the "Standoff" configurations, are not considered here.

Calculations of these configurations indicate that shock-driven collapse of the steel pipe causes some of the pipe to vaporize, resulting in an energetic flow of vapor. These also indicate the formation of a jet consisting of some of the pipe material that did not vaporize. The volume of the hole in the witness plate is considered a good comparative indicator of the energy in the condensate jet generated by the pipe collapse. The incident vapor flow is not thought capable of contributing much to the excavation process. These statements are supported later in this Section. Therefore, calculated jet energies will be compared with measured hole volumes as a test of the realism of the calculations. Table 2.1 lists the hole-volume statistics. It is seen that a considerable band of outcomes is observed from groups of seemingly identical experiments. This causes some uncertainty as to the "real" value of the hole volume, especially for the Pinex case, of which only two were employed and these used quite different pipe thicknesses.

The finding that the jetting in the Lead Wrap case was considerably more energetic than the Standard was quite unexpected. This configuration was thought to experience slower collapse and less-energetic jetting. However, the calculations described below are

TABLE 2.1 HOLE VOLUME STATISTICS FOR SYMMETRIC CONFIGURATIONS

	<u>Standard</u>	<u>Lead Wrap</u>	<u>Pinex</u>	
			<u>Thick Pipe</u>	<u>Thin Pipe</u>
Number of shots	8	3	1	1
Pipe Thickness, cm	.030	.030 + .203 (lead)	.071	.030
Average hole volume, cc.	17.8	39.6	61.5	25.
Standard deviation, cc	7.8	7.7	—	—
Experiment numbers	LS II - 1,2 LS III - 1, 10,11,14 LS IV - 1,2	LS II - 8 LS IV - 5,7	LS III - 20	LS IV - 17

consistent with the observations. The Pinex (thick pipe) result was even more surprising; the hole volumes for Standard, Lead Wrap, and Pinex were approximately in the ratio of 1 : 2 : 3. However, calculations and approximate theoretical considerations, described in Ref. 3, indicated that the 1 atm air present in the Pinex pipe had virtually no effect on the outcome; the result was attributed to the greater pipe mass. The thin-pipe Pinex result (LS IV-17), which lies well within the band of Standard results, bears this out. Further discussion of the mechanisms responsible for the various results, and their implications, will follow the calculational results.

The 2D Eulerian STREAK calculations described in Ref. 3 did not include the thin steel pipe. This approximation was thought to be reasonable at the time and allowed substantial savings in calculational costs. The findings of Ref. 3, however, suggested that the liner (pipe) must be represented. Test calculations with a simple geometry were then undertaken to determine the minimum zonal resolution required to give an adequate description of liner jetting. (These calculations, which are the steady-state results described in Appendix A, proved so informative that they were eventually performed for geometries representative of the Standard, Lead Wrap, and Pinex configurations.) It was found that the zoning requirements were less stringent than was previously thought. This is evidently a consequence of the use of a dual velocity in mixed cells in recent versions of STREAK. This allows slip flow along material boundaries and effectively minimizes the numerical diffusion responsible for an erroneous slowing of vapor adjacent to a solid wall which is characteristic of Eulerian codes. It also has the beneficial side effect of allowing a jet to initiate without being 5 or 6 zones in radial extent - this limitation had been experienced with Eulerian codes employing a single velocity in mixed cells.

The Standard and Lead Wrap configurations were then calculated with the initial configurations and zoning shown in Fig. 2.1. Subsequent rezones changed the axial but not the radial zoning; zoning

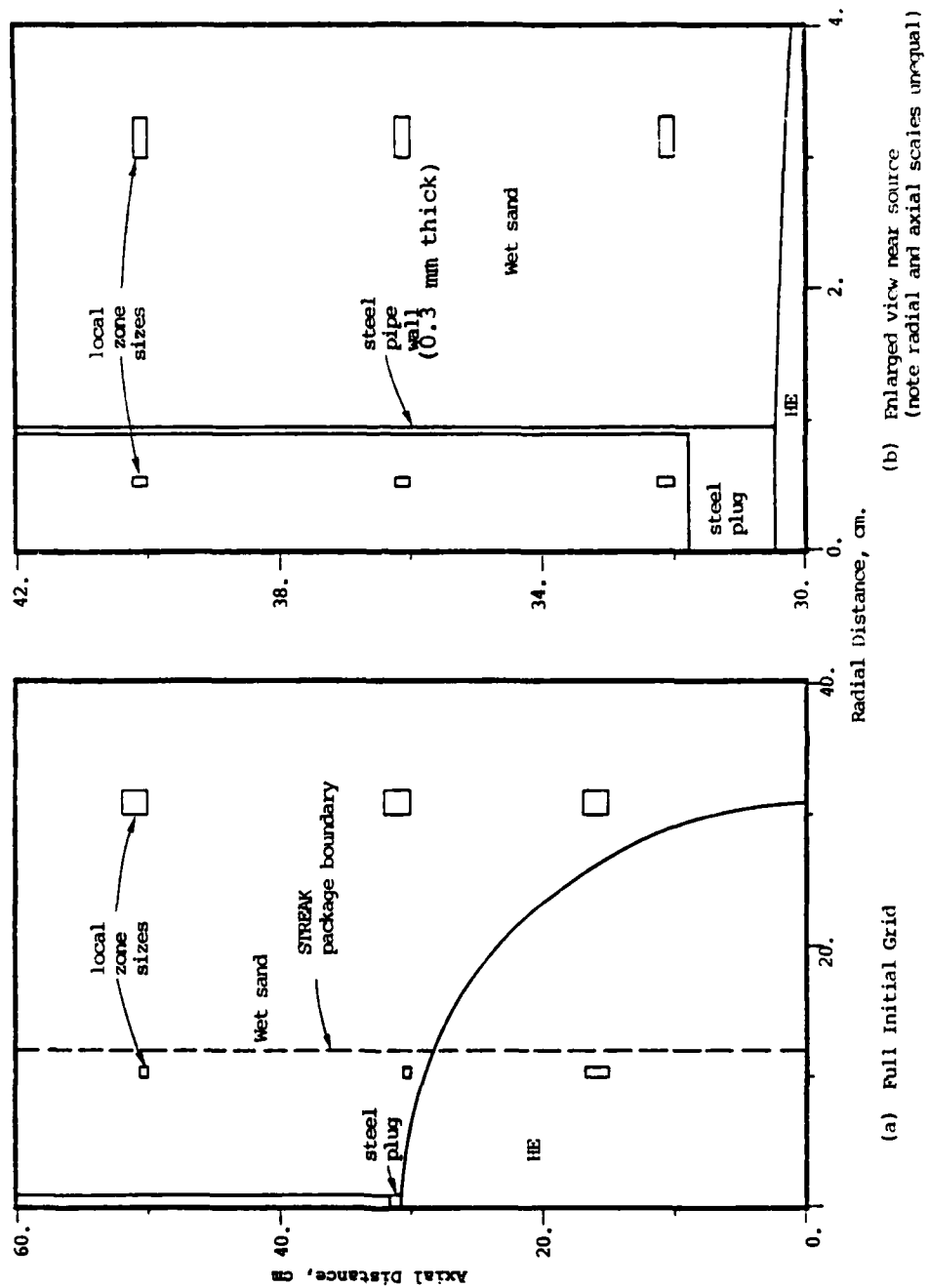


Figure 2.1 STREAK initial configuration showing zoning and package boundary

was never changed in the immediate vicinity of the collapse point or the ground shock. The calculations employed the "packaging" feature of STREAK whereby different regions of the problem, requiring different zonal resolution, are calculated in separate packages which communicate every cycle. In this manner the near-spherical flow some distance from the pipe could be treated with coarser zoning than that required in the pipe itself.

Figures 2.2 and 2.3 show the positions of the tracer strings defining the material boundaries at various times in the calculations. Both calculations indicate the formation of a jet of condensed material into the pipe ahead of the shock-driven collapse. Both also contain substantial iron vapor in the pipe which was generated by the energetic collapse of the pipe wall.* The vapor pressure also caused pipe expansion ranging to about 15 in the Standard calculation (Fig. 2.2). Very little expansion was seen in the Lead Wrap calculation because of the great mass of the lead; vapor pressures calculated were of the same order as those in the Standard case.

It is seen in Figs. 2.2, 2.3 that in the late stages of each calculation the tracer particles defining the material boundary between the steel pipe and the vapor in the pipe have developed a distinct choppiness. This is especially true at 128 μ sec in the Standard case, where the calculation was stopped. The source of this difficulty is that the thickness of the undisturbed pipe is only about one-third of the local radial zone size. Where a material region is so poorly resolved the algorithms used in describing tracer velocity and mixed cell pressure will occasionally combine to produce erratic tracer motion

* Liner material vaporized by collapse-induced heating is transferred across the tracer string into the open pipe. Details of the technique are described in Ref. 9.

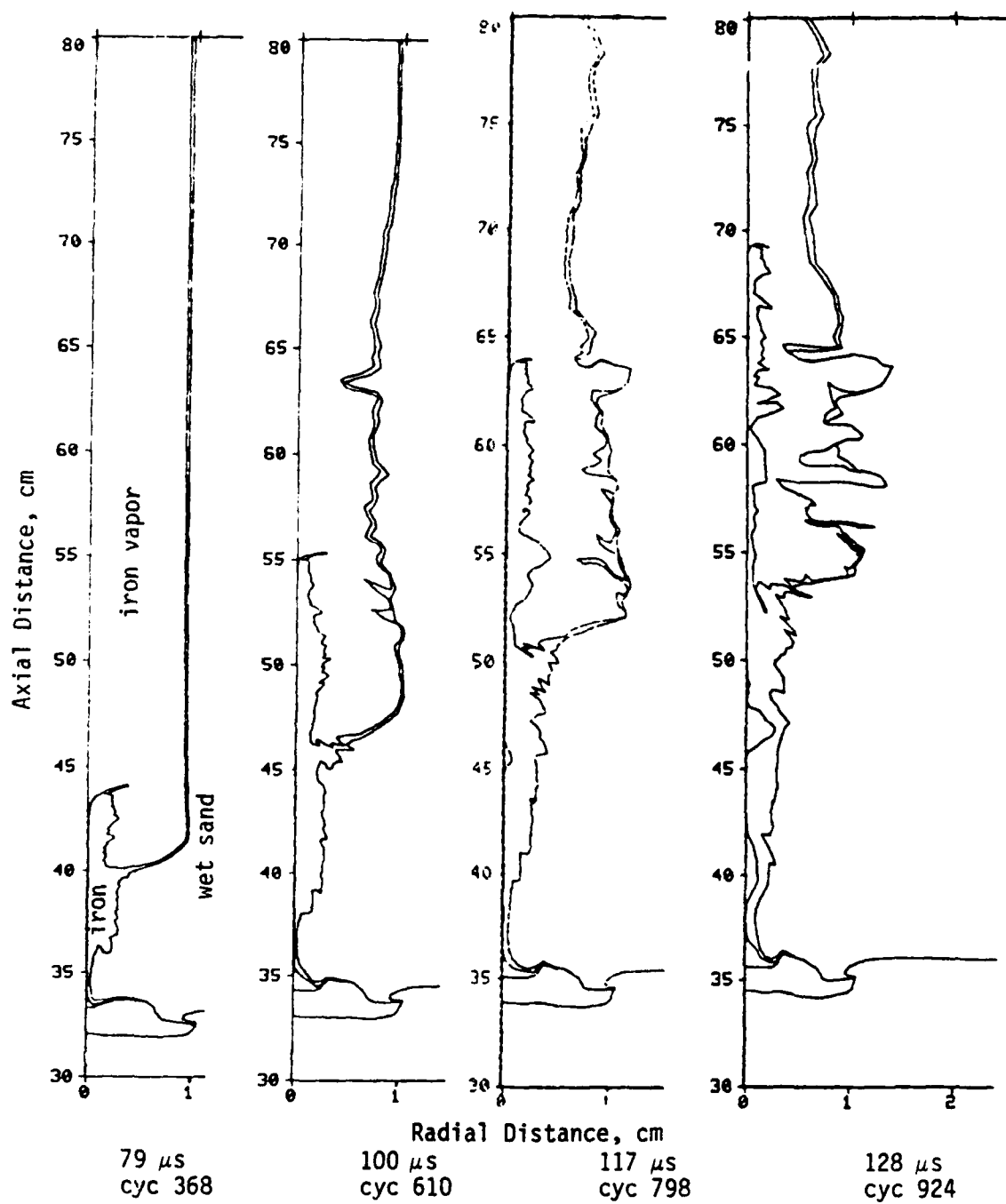


Figure 2.2 Evolution of the pipe collapse and particulate jet in the calculation of the PI Standard configuration.

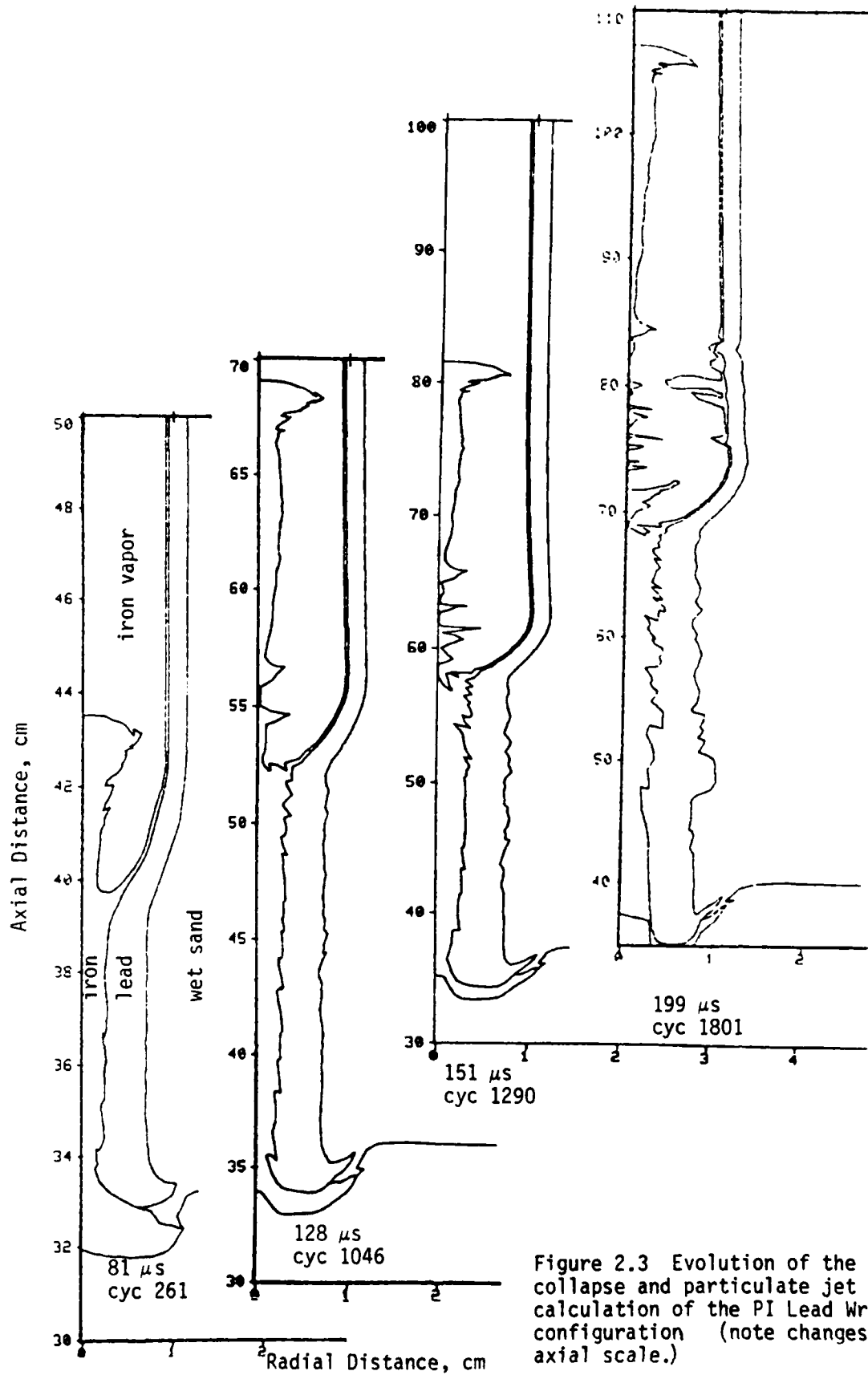


Figure 2.3 Evolution of the pipe collapse and particulate jet in the calculation of the PI Lead Wrap configuration (note changes of axial scale.)

at a vapor/solid boundary.* After examination of the calculational edits, we believe the Standard results are credible until just before 128 μ s and the Lead Wrap results until at least 199 μ s. The comparison of jetting energies described below is based on values which leveled off before these times. Furthermore, the condensate jet and the vapor are formed near the collapse point, away from the tracer difficulty. The tracer difficulty involved radial velocities of at most several hundred m/sec, more than an order of magnitude lower than the axial velocities in the problem.

Two useful quantities for comparison are the calculated energy in the condensate jet and in the vapor. These are shown as functions of time in Figs. 2.4 and 2.5. The plot for condensates shows kinetic energy only; their internal energy is much smaller and is not thought to contribute to penetration of the witness plate. The calculated jet energy for the Lead Wrap levels off at about 68.5 KJ in 5.1 g, vs about 36 KJ in 3.2 g for the Standard. The vapor energy (internal plus kinetic) is larger for the Standard, apparently because of the higher collapse velocity. The calculated jet velocities may be compared with jet velocities inferred from the data. The witness plate on LS III-14, a Standard configuration, contained diagnostic pins at several depths to indicate the time scale of growth of the hole. These data are shown in Fig. 2.6 along with vapor arrival data from this and several other pipes on LS III. It is strongly suggested from the data that

* These algorithms are described in Ref. 12. Briefly, tracer velocities are interpolated from cell centers; mixed cell pressure is determined by volume-weighting of the component pressures. Unless very closely spaced tracers are used to describe such a thin strip of material as the pipe wall, radial motion may at times cause the tracer strings describing opposite sides of the strip to attempt to cross. The automatic tracer sorting routine responds by combining the opposite sides locally. This results in a high density in that material which can, in extreme cases, produce an anomalously high cell pressure which "kicks" some of the solid material into the available low-density region.

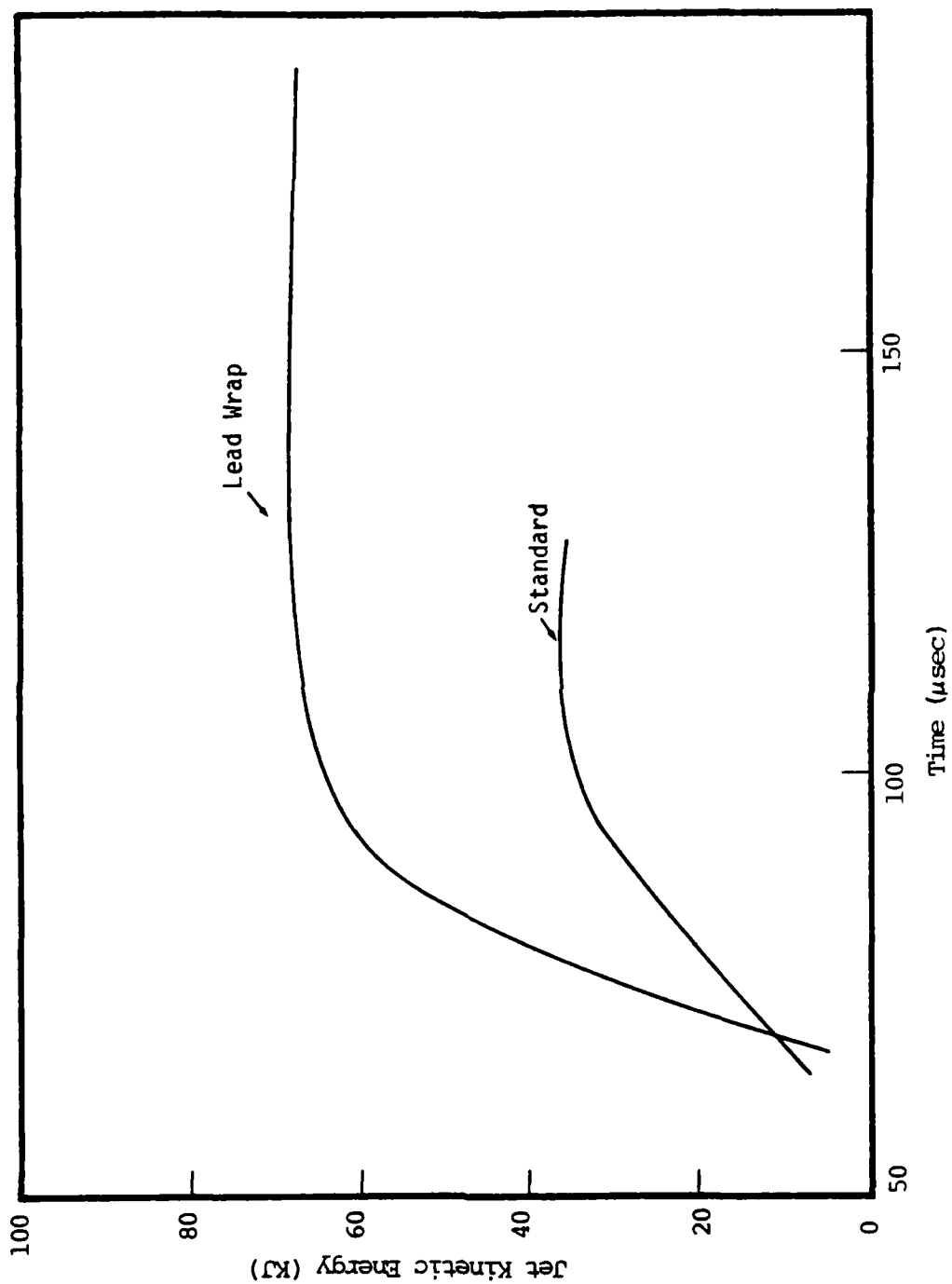


Figure 2.4 Growth of kinetic energy in the particulate jet.

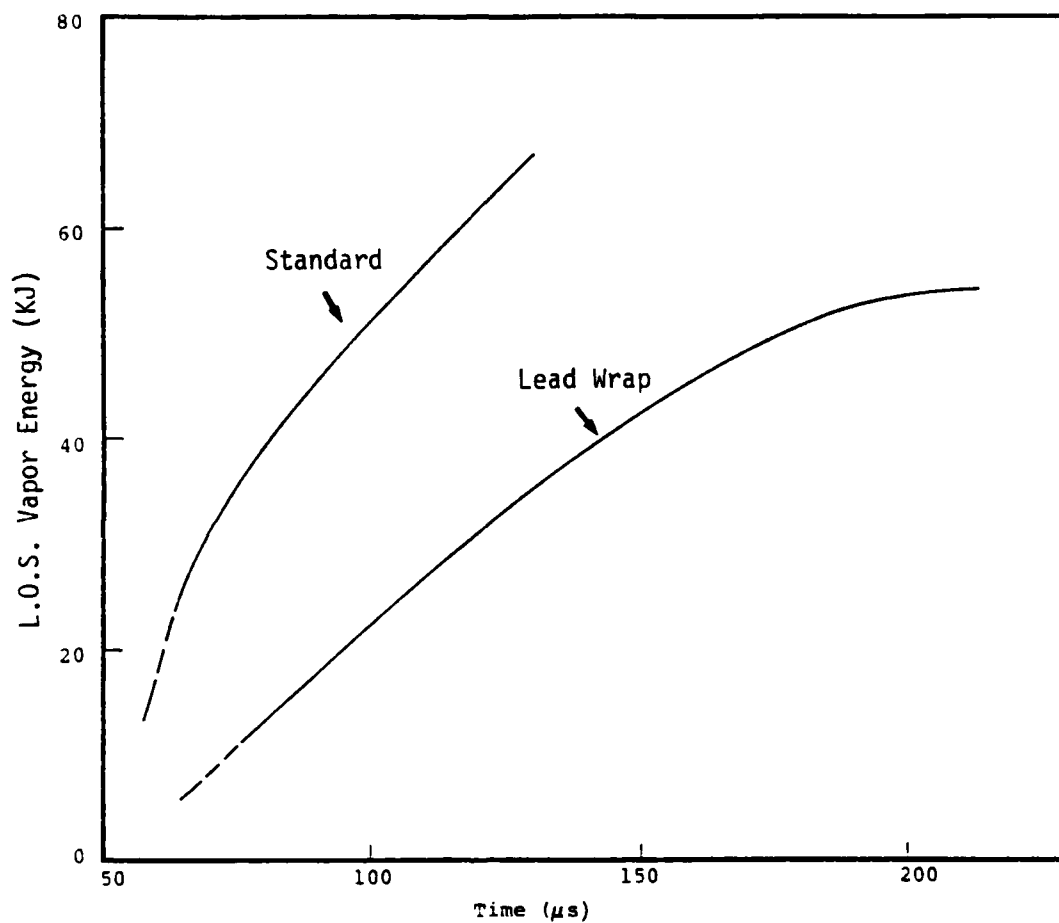


Figure 2.5 Growth of total energy in the vapor ahead of the collapse point.

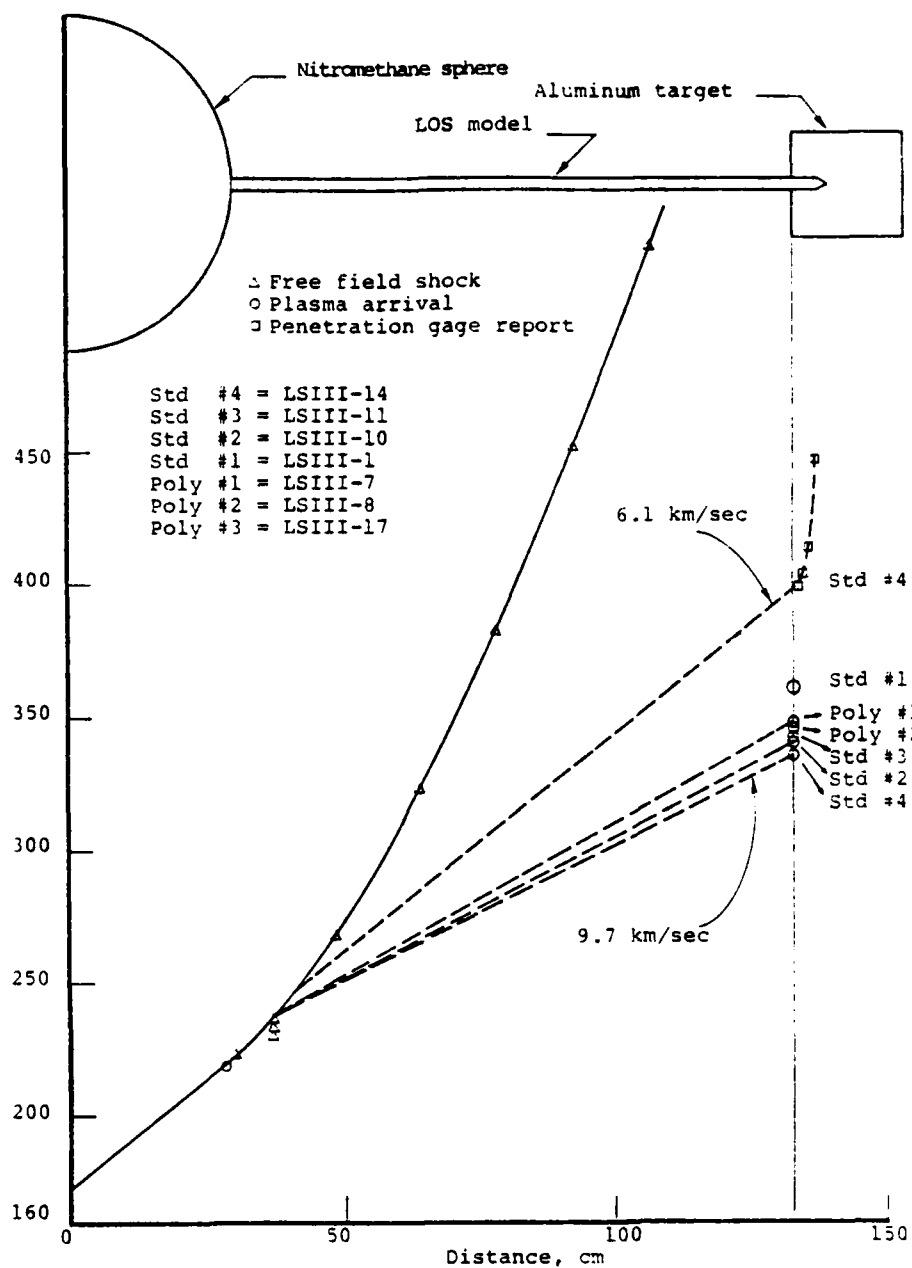


Figure 2.6 Arrival and penetration data from Standard and Polyolefin spiral configurations of LS III.

the hole formation is too late to be attributed to the vapor arrival. It is made by something which travels at an average speed of about 6 Km/sec, which compares well with the calculated velocity of about 5.5 Km/sec for the leading edge of the jet. The evidence of vapor arrival in the Polyolefin Spiral configurations LS III-7,8 (at about the same time as in the Standard case, Fig. 2.6), which produced no significant damage to the target plate, also supports the claim that particulates make the hole. The calculated vapor front arrival is also indicated in the figure. Although the calculation was not continued until the formation of a reflected vapor shock at the witness plate, it is evident that the calculated velocity of the front is consistent with the arrival data.

It is postulated that the condensate jet makes the observed hole by impact cratering. There are considerable data on craters made by hypervelocity impact of single particles, of the order of 1mm diameter or larger against a target. In the present experiments the impacting condensates are almost surely a shower of much smaller particles, probably both solids and liquid droplets. Nevertheless, it is reasonable to look for a correlation between the hole volume and the impacting kinetic energy. The calculated and experimentally-inferred jetting velocities lie in the range of about 5 to 6 Km/sec. Various literature on hypervelocity impact cratering⁽⁴⁻⁶⁾ suggests that the ratio of hole volume to impacting energy is a weak function of particle velocity. Therefore, it is reasonable to require the ratio of jetting energies calculated for two configurations to be comparable to the ratio of the observed hole volumes. The average hole volumes observed for the Lead Wrap case are about 2.2 times the average observed for the Standard. The ratio of the calculated maxima of E_{jet} is 1.9, which is considered to be well within the experimental uncertainty.

A quantitative comparison with hypervelocity data is also interesting. For iron incident on aluminum, it may be inferred from

empirical relations found in Ref. 4 that the ratio of hole volume to impacting energy is $V/E \approx 2$ to 3 cc/KJ . This would lead one to expect hole volumes of about 70 to 110 cc for the Standard configuration and 140 to 200 cc for the Lead Wrap. These values are about 3.5 to 5 times the observed volumes. This is not surprising, since exact correspondence with the single particle data is not to be expected; linear superposition is not credible. If the calculations are taken at face value, this would imply that a shower of tiny particles has cratering efficiency several times lower than a single particle. This is plausible in view of interactions between the particles and the fact that some particles will collide with crater ejecta. The principal finding of this exercise is that the variation in calculated jet energy for the different configurations correlates very well with the observed variation in target damage. The variation of calculated vapor energy, on the other hand, does not. The calculated E_{vap} is actually lower for the Lead Wrap case.* This is plausible because of the lower collapse velocity. Vapor energy should not be expected to correlate well with target damage. It is difficult to postulate a plausible mechanism by which vapor impact would make a hole just the same size as the pipe, when pipe rupture surely accompanies the reflection of the incident vapor flow at the witness plate.

The calculational results are seen to be consistent with the experimental results. However, it is necessary to try to understand the results in terms of physical mechanisms. The steady-shock calculations for the configurations (Appendix A) proved quite useful in this regard. They produced the unexpected result that all three

* The original expectation that the Lead Wrap would be beneficial was based on calculational studies indicating that the use of extra mass around the pipe near a nuclear source would result in lower-energy vapor flow. Symmetric distribution was indicated to be at least as good as asymmetric distribution (Refs. 13,14). This was one reason for including the Lead Wrap configuration in the experiments.

configurations jet energy at the same rate when driven by identical steady shock conditions, once the transient features have decayed. This result was then explained by a modification of Birkhoff's simple jetting theory - see Appendix A. Therefore, the observed differences when driven by a decaying shock must be due to nonsteady effects. Furthermore, any explanation must be consistent with the steady state findings. As a result of this requirement an explanation that originally seemed pleasing had to be discarded (the scenario of Ref. 3 which resulted from an inappropriate application of steady state jetting theory).

The postulated explanation is based on ground shock decay. Decay is rapid; when an element reaches the axis the driving pressure field is significantly lower than when the element was first driven. The pressure experienced by the element at convergence on axis is related as much to the initial driving conditions as to the current pressure in the ground around the element, and a finite time is required to adjust to the current ground pressures. This time is longer in the Lead Wrap than in the Standard because of the thickness of the imploded lead and the lower sound speed in lead. The longer duration of the high convergence pressure in the Lead Wrap case is confirmed in the calculational edits. The jet formation is better "tamped" in the Lead Wrap case than in the Standard.

This argument also explains why the particulate jet is more energetic in the thick-walled Pinex (LSIII-20) than in the Standard. However, it does not explain why the jet is more energetic in the Pinex than in the Lead Wrap; the Pinex would appear able to adjust to reduced driving pressure more rapidly than the Lead Wrap. Nevertheless, even though only one such Pinex configuration was used, the data suggest a high probability that it produces more energetic jetting than the Lead Wrap. In the absence of a Pinex calculation a possible explanation is offered. Because of the smaller implosion velocity experienced by the Lead Wrap, an element of liner initially at a given

station reaches the axis later and farther behind the decaying shock front than the corresponding element in the Pinex. Consequently, the average driving pressure experienced by it during implosion is less and the jetting energy lower, despite the longer time required to reduce the convergent pressure to that of the surrounding ground. It would be very useful to perform a calculation of the Pinex configuration, when time and budget constraints permit, for the insight it is likely to provide.

In conclusion, the calculations and phenomenological explanations now appear to be consistent with the experiments. Unfortunately, it was not possible to obtain such satisfactory agreement without inclusion of the thin pipe wall in the calculations. Implications of this for the nuclear case are discussed in Section 4.

Other symmetric configurations are worthy of comment although they have not been calculated, in particular, LSII-6, 9, 10 which employed polyolefin, glass, and cardboard liners inside the Standard steel pipes (Table 1.1). These liners had considerably less mass than the pipe walls. Therefore, the collapse dynamics should be very similar to that of the Standard case; the hole volumes in the witness plates should also be very similar. All three hole volumes lie within the spread of the Standard results (although glass and polyolefin liners produced slightly deeper holes). In fact, the Standard hole volume statistics available at the writing of Ref. 3 (LSII, III) were virtually indistinguishable when these three liner cases were included: 19.8 ± 7.9 cc excluding them, 19.8 ± 8.2 cc including them. These results are consistent with the above discussion. It is not clear, of course, what role the liners play in the jetting dynamics.

SECTION 3

ASYMMETRIC CONFIGURATIONS

The experiments with asymmetric configurations also produced major surprises. The failure of external spiral asymmetries to have any significant effect, even if the spiral was made of lead, was completely unexpected. On the other hand, the ability of a thin metal or even plastic spiral loosely inserted inside the pipe to suppress all significant damage to the target plate was equally surprising.

It is clear that the internal spiral performs its "miracle" by some mechanism quite different from the mass asymmetry which was naively thought significant in the early days of this research effort. It is indicated that the internal spiral prevents jetting by either (a) the blockage of the particulate jet at its source in the pipe collapse region or (b) the scatter of jetted particulates by the spiral downstream. The latter is favored by the body of data summarized in Table 1.1. In particular, note that an internal spiral in the last 0.38 m of pipe (LS IV-8,9) was essentially as effective as those going the full length, whereas spirals limited to the first 0.15 to 0.30 m were only partially effective. "Standoff" experiments (LS III-2, 3, 4 and LS IV-20E) suggest that the large majority of the energy of particulate jetting is injected into the pipe in the first 0.50 m or less. The symmetric calculations suggest the same thing. Taken together, these facts support mechanism (b).

The next question is, how can such thin spirals, resting flat against the pipe wall, so completely protect the target plate? The difference between the vapor and particulate velocities suggests an answer. Both data and calculations for the Standard configuration indicate velocities of about 10 Km/sec for the vapor front and 6 Km/sec for the leading edge of the particulate jet. Thus, the vapor can interact with the spiral for a time before the particulates arrive

and this time increases with range from the HE. This observation, combined with the fact (long overlooked in the attempt to understand the observations) that the spirals are loosely inserted in the pipe, not attached to it, suggests the possibility of a significant effect of vapor on the spiral. It is postulated that the fast vapor stagnates against the leading edge of the spiral and forces it away from the pipe wall. This then becomes an obstruction to the flow which magnifies the twisting tendency of the aerodynamic forces.

It is easy to demonstrate with an approximate analysis (see Appendix B for details) that the aerodynamic forces and the time available are sufficient for considerable turning to occur before the arrival of the slower penetrating materials. The vapor arrival precedes the particulates of the jet at the end of the pipe by about $60\mu\text{s}$ in the Standard case. Stagnation pressures up to about 10 kbars are available to twist the spiral insert. It is estimated that between 80 and $90\mu\text{s}$ is the time required to turn the wide face of the spiral perpendicular to the flow. During the $60\mu\text{s}$ available before particulate arrival this analysis suggests the spiral will turn about 15° and protrude into the pipe about 5 mm. It is noteworthy that the 2 mm x 2 mm lead helical baffles in the last 0.38 m of pipe in test LS III-12 provided almost complete protection to the witness plate.

It appears that the relatively thin spiral can act as a "meteor bumper" to deflect or vaporize particulate matter which would penetrate the target plate and produce a noticeable crater if earlier impact did not occur. It is believed that most particulates pass near the wall at some stage of their trajectories to the witness plate, otherwise the necessary protrusions would need to be a larger fraction of the pipe radius.

This mechanism is consistent with the observation from test LS IV-22 in which a 0.51 mm steel spiral replaced the 0.36 mm plastic spiral which had been used earlier. This experiment used a spiral in

only the first 0.30 m of pipe. Data extrapolations from plastic spirals in the first 0.15 and 0.23 m (LS III-15, 16) had suggested that this limited spiral would suppress the jet completely. However, a hole volume of nearly half the average produced by the Standard pipes (and almost as large as the smallest hole of the Standard set) was actually observed in the witness plate. It is suggested that this result follows from the relatively high density of iron compared to plastic. The analysis of Appendix B finds that the rate of increase of turning angle, $\dot{\theta}$, is proportional to $\Delta L^{-2} \rho_H^{-1/2}$ at low θ , where Δ is the thickness of the spiral insert, L its width in the axial direction, and ρ_H its density. As a result the steel spiral turns through a smaller angle in the limited time available. The smaller turning probably means decreased effectiveness.

The physical blockage of the pipe by the warped spiral should have some effect on the vapor, in addition to stopping the particulates. Unpublished data from LS IV (not yet fully reduced at this time) suggest that, while first arrival of the vapor at the target plate is only slightly delayed by the spiral (as found in the LS III comparisons cited in Section 2), the spiral can cause a sizeable reduction in the vapor impulse. This is supported by data from the nuclear event Flora (Section 4).

In summary, the proposed scenario explaining the role of the spiral in terms of an aerodynamic twisting mechanism appears to be consistent with the entire body of data acquired to date by PI. The planned LS V experiment will contain some specific tests of this scenario. For example, there will be pipes in which the spiral is solidly attached to the wall. Whether the ultimate scenario is the one proposed or some other, its data base should be sufficient to permit more confidence in it than is now possible.

SECTION 4

IMPLICATIONS FOR UNDERGROUND NUCLEAR TESTING

There is now more basis for conjecture on underground test implications than existed at the writing of Ref. 3 because of the execution in 1980 of the nuclear test Flora by the Los Alamos National Laboratory. This test included an experiment to determine whether a spiral insert would slow the fast plasma sufficiently to increase the time available before shock-induced destruction occurred in certain electro-optical equipment. Two 15 cm diameter, 20 m long tubes were installed. These were identical except that one contained a steel spiral insert scaled approximately from those used in the PI simulations.

The spiral insert had a significant, favorable effect on the plasma flow in Flora (Ref. 7). Slifer cables showed the gradual development of a lag in first arrivals with range in the asymmetric pipe. Pressure histories recorded at 18 m indicated plasma arrival at about 0.72 ms in the smooth pipe with a peak pressure of about 2.5 kbars; in the asymmetric pipe the arrival was at about 0.82 ms with a peak of about 1.3 kbars. Only the first plug* was penetrated in the asymmetric pipe; three plugs were penetrated in the smooth pipe. It had been suspected, prior to the shot, that the spiral would expand with the pipe, rupture on expansion, and not be as effective as in the PI configurations. This was apparently not the case. The key to the success of the spiral on Flora, as in the PI cases, may well be that the spiral was not attached to the pipe.

* At the end of each pipe was a sequence of three plugs (Al plates) at about 23 cm intervals, the first 1.27 cm thick, the second 2.54 cm, and the third 3.81 cm. Penetration was indicated by shorting of the TDR cable behind the plug which could be caused by vapor pressure or by failure of the plug.

The primary observed effect of the Flora spiral was on plasma flow. Its effect on particulate jetting is unknown, and the contribution of particulates to plug penetration is not known. On typical HLOS tests particulate jetting is thought to be an even more severe threat to the samples than the plasma. Therefore, it is important that nothing impede the spiral's function as a stopper of particulates. According to calculations, the energetic plasma flow in the LOS causes substantial pipe expansion while the flow in the PI simulations does not. Calculated LOS expansion in the nuclear case is usually well in excess of the 30% believed to cause pipe rupture. A concern with the use of spirals in LOS tests is that the ability of the spiral to stop particulate jetting has not been demonstrated when major pipe expansion occurs. Therefore, the normal requirement to minimize energetic plasma flow appears completely compatible with the use of a spiral. Obviously, there is a point at which further reduction in the plasma flow would be undesirable, if the spiral works as we suggest. But there is no evidence that this level is attainable in practice. The prompt plasma flow for Diablo Hawk was the most benign ever calculated or measured, but the calculations indicate that it caused appreciable pipe expansion while the PI simulations did not. Specific applications of the approximate "twisting" model of Appendix B suggest that the prompt plasma flow calculated for Diablo Hawk could turn a spiral perpendicular to the flow prior to the arrival of particulate jetting, at least to a range of the order of 50 m. (This assumes a spiral whose width equals its radius.)

The symmetric Lead Wrap results were quite unexpected because of earlier classified parametric studies indicating the superior performance of dense, long extensions. The earlier work used plasma energy as the primary figure of merit; the threat associated with the Lead Wrap configuration is thought to be jetting particulates. (Recall that the Lead Wrap calculation described in Section 2 predicts vapor

energy 30% less than the Standard calculation as well as later arrivals, which is consistent with preliminary pressure history data from the LS IV-5,7 Lead Wrap pipes⁽²⁾.) The question arises whether the Lead Wrap results have adverse implications for dense extensions. The answer appears to be that they do not. Even the longest extensions used to date are limited to the near-source region, whereas the PI lead wrap went the full length of the pipe. A well-designed extension is overtaken by the ground shock-driven closure while the energy in the LOS is still low. The ground shock pressures at the ends of the Mighty Epic, Diablo Hawk and Miners Iron tuballoy extensions were approximately the same as the driving pressure at the PI source. Hence, the two situations are not directly comparable. The calculation-based understanding of the LOS results is consistent with data, as is the calculation-based understanding of the PI symmetric results. Most importantly, dense extensions have performed well. Therefore, the conclusions of the earlier parametric study are still thought to be valid. It is speculated here that a short Lead Wrap near the source in a PI simulation would result in no more jetting than the Standard case and quite possibly less.

Certainly, extension designs have not yet been optimized. The Miners Iron LOS flow was more energetic than expected. It is recommended that further optimization studies include some LOS closure calculations which represent the thin pipe wall which appears to be important in the PI simulations. This would be useful in determining whether the use of dense extensions to minimize plasma flow causes locally-enhanced particulate jetting. If it does, a spiral insert should be able to control it. It is not clear that greater realism would be achieved by including the pipe wall beyond the extension unless pipe expansion is insufficient to rupture the pipe. In a case where major rupture is indicated, the particulate jet could in reality consist mostly of the exposed grout.

SECTION 5

CONCLUSIONS AND RECOMMENDATIONS

The following conclusions are based on the experimental data and insight gained from the calculations:

- The damage to the witness plate appears to be due to the jetting particulate matter, the primary source of which is the steel pipe.
- 2D Eulerian calculations of the symmetric configurations appear to produce jetting results consistent with the comparative damage levels observed on the Standard and Lead Wrap experiments, provided the thin steel pipe wall is explicitly included in the calculation.
- The success of internal spiral asymmetries in preventing damage to the witness plate and the relative damage levels observed in various configurations using such asymmetries in only a portion of the pipe are consistent with the postulate that the spiral is separated from the wall by the precursor vapor flow and acts as a "meteor bumper" to deflect or vaporize hypervelocity particulate matter.
- The use of internal spiral asymmetries in nuclear LOS events has great potential for drastically reducing damage to closures or experimental objects caused by particulates and for eliminating the need for other hardware to prevent such damage. It also has significant potential for delaying and reducing plasma flow.

In addition to the above, the following observation has been so persistently valid throughout this work that it warrants inclusion in the above list:

- The understanding of experimental results is greatly enhanced by the attempt to perform calculations, even if these are initially inconsistent with the data; and the results of calculations of complicated phenomena are highly suspect unless they have been compared with relevant data. Experimental and theoretical work advance hand in hand. The greatest progress comes in attempting to reconcile experiments and calculations; for example, the spiral mechanism now appears to be very different from that initially imagined when inertial effects were expected to dominate.

The following recommendations are also offered:

- An internal spiral asymmetry should be tried on a nuclear LOS event as soon as possible. Its design should be carefully based on the experimental findings and phenomenological understanding obtained from the PI simulations.
- Continuing calculational studies of nuclear LOS closure performance should include some calculations in which the thin pipe wall is explicitly represented.

REFERENCES

1. Moore, E.T., Jr., and Funston, R., "Asymmetric Collapse of LOS Pipe", Physics International Reports, DNA 5023F, July 1979 (for LS-II) and DNA 5322F, May 1980 (for LS-III)
2. Moore, E.T., Jr., and Funston, R., Results of experiment LS IV, 1979-1980 (private communication not yet published).
3. Barthel, J.R., "LOS Energy Flow Simulation", Section 5 of S³ Final Report on Late Time Containment, DNA 5293F, April 1980.
4. Bjork, R.L., "Review of Physical Processes in Hypervelocity Impact and Penetration", Proc. 6th Symposium on Hypervelocity Impact, Vol II, Part 1, August 1963 (also appeared as RAND Corp. RM-3529-PR, July 1963).
5. Wagner, M.H., Brooks, N.B. and Bjork, R.L., "Impact of Porous Al Projectile on Al at 20 and 72 Km/sec", Proc. of 7th Symposium on Hypervelocity Impact, Vol III (Theory), February 1965.
6. 7th Hypervelocity Impact Symposium, Vol V (Experiments), Feb 1965
 - a. Palmer, E.P. and Turner, G.H. "Energy Partitioning in High-Velocity Impact Cratering in Lead",
 - b. Halperson, S.M., "Comparison Between Hydrodynamic Theory and Impact Experiments".
7. Eilers, D., LANL, unpublished presentations of data from the Flora nuclear event, 1980.
8. Sedgwick, R. S³, private communication.
9. Duff, R.E., Peterson, E.W., and Barthel, J.R., "Late Time Containment Research", S³ Final Report, DNA 4908F, March 1979.
10. Birkhoff, McDougall, Pugh, and Taylor, Journal of Applied Physics 19, p 563, (1948).
11. Birkhoff, G. and Zarantonello, E.H., "Jets, Wakes and Cavities", Academic Press, 1957.
12. Bailey, L.E. Jr. and Baker, J.C., "The STREAK Code", S³ Topical Report, in preparation, to be published 1981.
13. Rimer, N. and Barthel, J.R., "Effects of Asymmetries in Line-of-Sight Nuclear Tests", S³ Topical Report SSS-R-75-2672, July 1975.
14. Rimer, N., Wiehe, J.W., and Barthel, J.R., "Effects of Pipe Wall Mass Distribution in Line-of-Sight Nuclear Tests", S³ Topical Report SSS-R-78-3744, August 1978.

APPENDIX A

CALCULATIONS OF JETTING WITH A STEADY SHOCK

Calculations of jet formation in the frame of reference of an assumed steady shock wave were initially undertaken as an economical way to determine the zoning requirements for calculations of the actual decaying-shock configuration including adequate resolution of the liner. The results proved to be so useful that the Standard, Lead Wrap, and Pinex configurations were all calculated in this manner. These calculations, performed with the STREAK code, produced some unexpected findings, which were later explained in terms of a simple theoretical model. The model even gives reasonable quantitative agreement with the calculations. Any scenario developed for the performance of the actual decaying-shock configurations must be consistent with the insights derived from this exercise.

Conditions selected for the calculation were taken from a previous calculation for the PI Standard configuration just beyond the range where pipe collapse on axis first occurred. (That calculation did not include the steel liner.) The shock conditions were: pressure $P_s = 119$ kbar, density $\rho_s = 2.7187$ g/cc (wet sand), specific internal energy $e_s = 7.9 \times 10^9$ erg/g. With ambient density $\rho_0 = 2.0198$ g/cc this corresponds to a shock velocity of $V_s = 4.785$ km/sec. The material behind the shock has velocity $u' = 3.555$ km/sec in the shock frame of reference. Fig. A.1 shows the configuration and the zoning. The above values of ρ_s , e_s , and u' were imposed at the top and right of the grid at all times. In this frame of reference and orientation the jet goes out the top of the grid.

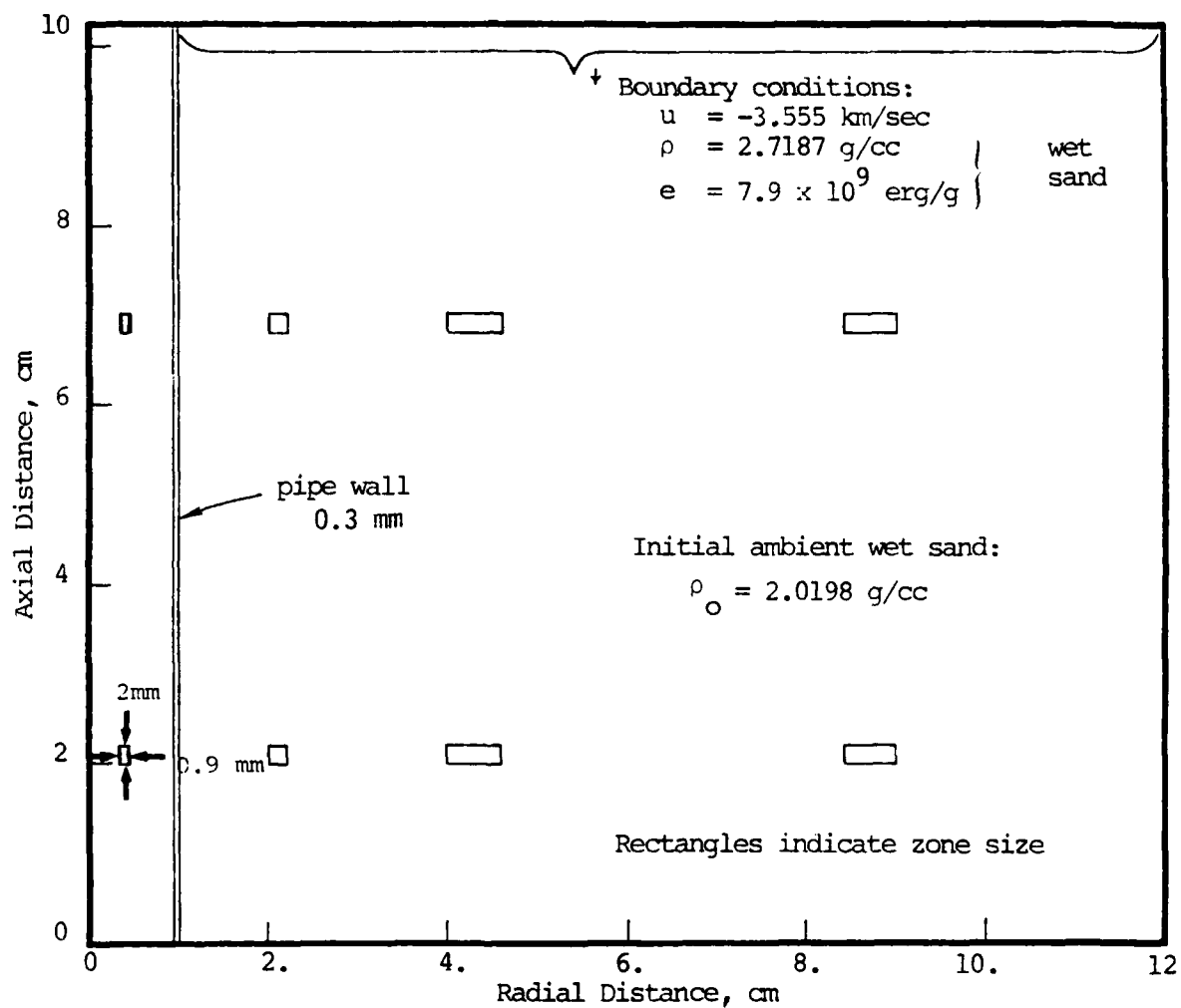


Figure A.1 Initial configuration for calculations in steady shock frame of reference.

The zoning was employed on a trial basis and was not expected to be adequate for jet formation. Previous experience of other investigators with jetting calculations using the HELP code had produced a rule of thumb requiring at least 5 or 6 zones radially across the jet if it is to form.⁽⁸⁾ The present finding that two zones is sufficient has tentatively been attributed to the use of a "slip velocity" in mixed-material cells in STREAK; each material has its separate velocity. This minimizes the numerical diffusion inherent in Eulerian codes.

Four calculations were carried out: the Standard configuration, the Pinex configuration (thicker wall, plus 1 atm ambient air in the pipe), the Lead Wrap configuration, and a more-finely zoned version of the Lead Wrap - to assess the influence of zoning. The calculations were started with the pipe at its original radius everywhere and carried until a steady flow configuration with jetting was achieved.

It is useful to compare the mass and energy moving ahead of the collapse point in these calculations. After steady flow is achieved, the rates of mass and energy flux out the top of the grid may be compared. (This is a more convenient quantity to edit). Figs. A.2 and A.3 show the mass in the jet and the mass in the vapor that have gone out the top as functions of time. The vapor is made at the collapse point. Liner material is vaporized as required by collapse-induced heating. The mass vaporized in this manner at each cycle is transferred across the tracer particle string defining the material boundary (technique described in Ref. 9). It is noteworthy that the asymptotic mass flux rate into the jet, \dot{M}_j , is nearly the same in all calculations. This result, which was at first surprising, is consistent with a simplified theory of jetting - see below. (The fine-zoned Lead Wrap case was not carried far enough for this comparison; it was useful only in demonstrating that the coarser zoning provided an adequate description of the jetting).

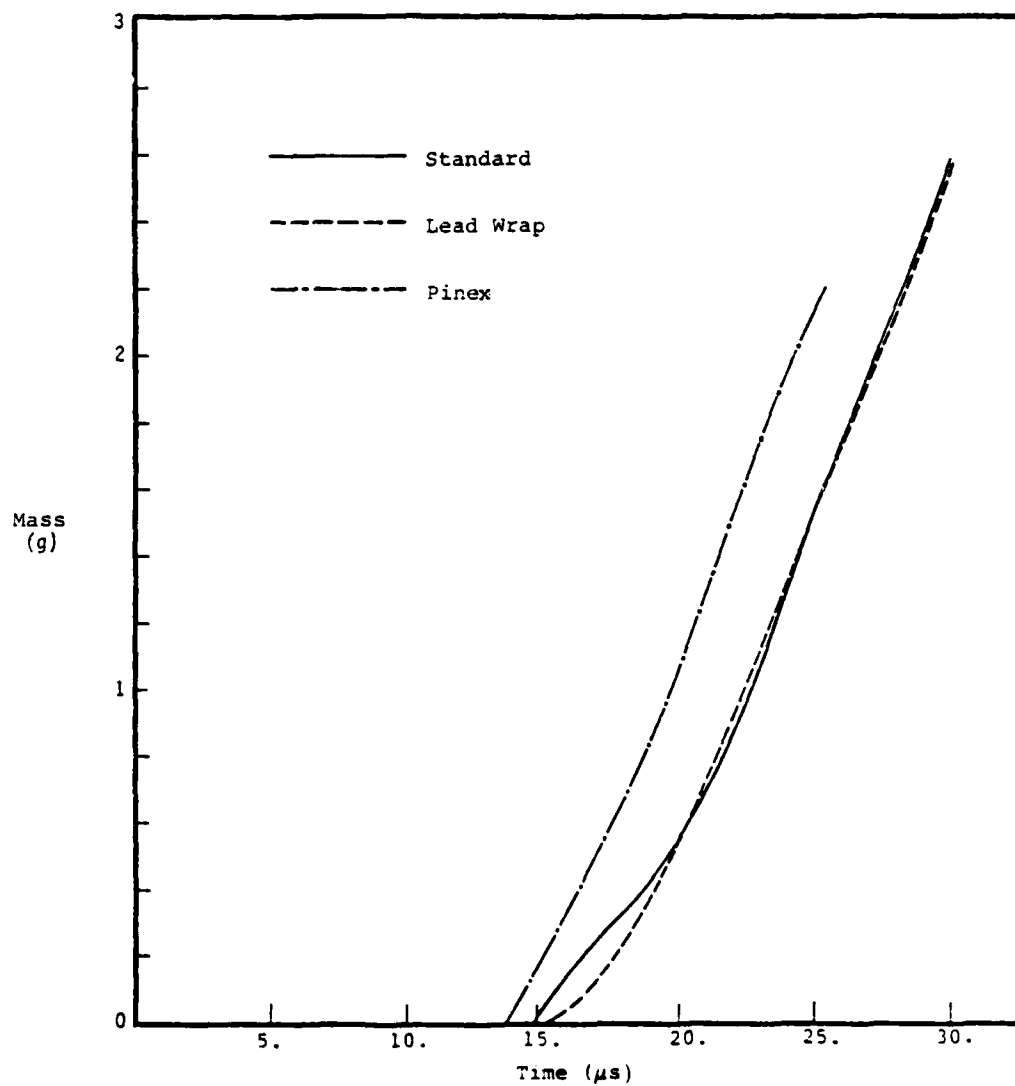


Figure A.2 Condensate mass flux out of the computational grid

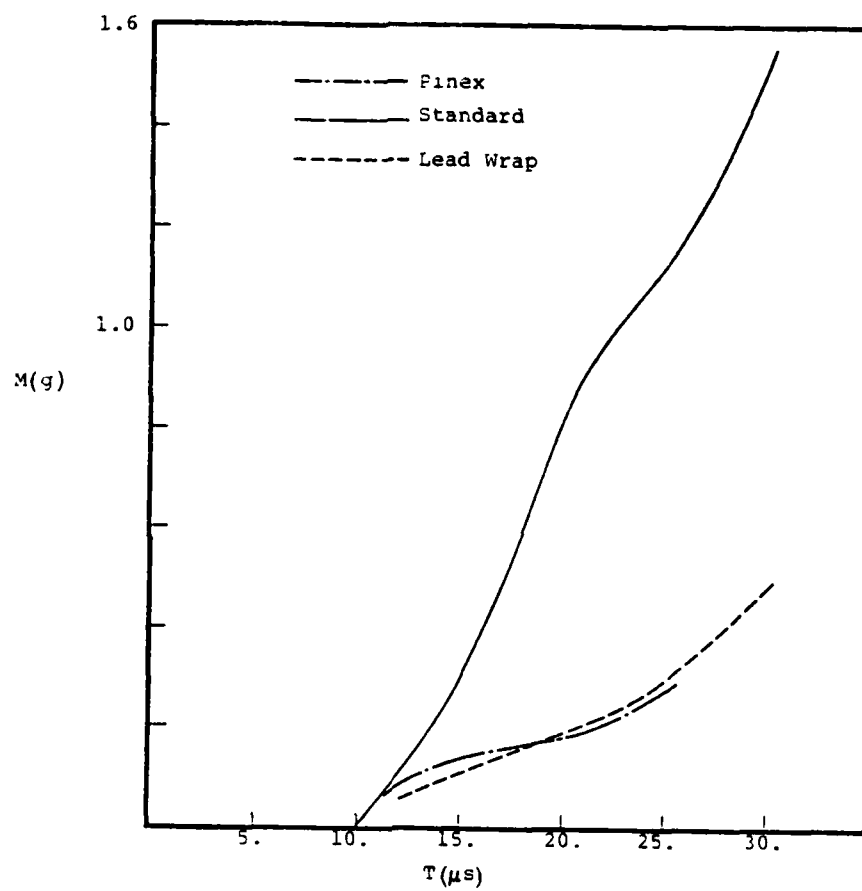


Figure A.3 Vapor mass flux out of the computational grid.

The plots of energy out the top of the grid in the jet and in the vapor, Figs. A.4 and A.5, have the same character as the mass flux plots. The energy flux rate, \dot{E}_j , for the condensate approaches nearly the same value in all, again consistent with the simplified theory.

In order to explain the phenomenon of equal \dot{M}_j and \dot{E}_j for different configurations, it is necessary to digress and review the impulsive-jetting theory of Birkhoff, et al^(10,11). Refer to Fig. A.6 which depicts a detonation wave propagating through a high explosive surrounding a thin liner. A steady state exists in the frame of reference moving with the apex. In this frame u_ℓ is the detonation velocity, v_1 the velocity of material toward the apex, and v_o the impulsive velocity imparted to the liner by the HE. The "impulsive" approximation is based on the rapid relief of pressure behind the detonation wave because of expansion. v_a is the velocity of the apex in the laboratory frame. For simplicity, we need consider only the cylindrical pipe case ($\alpha = 0$).

The following expressions apply (see vector diagram in Fig. A.6):

$$v_o = 2u_\ell \sin \frac{\beta}{2} \quad (A.1)$$

$$v_1 = u_\ell \quad (A.2)$$

$$v_a = u_\ell \quad (A.3)$$

The steady state assumption permits the Bernoulli Equation to be used:

$$e + \frac{p}{\rho} + \frac{u^2}{2} = \text{constant} \quad (A.4)$$

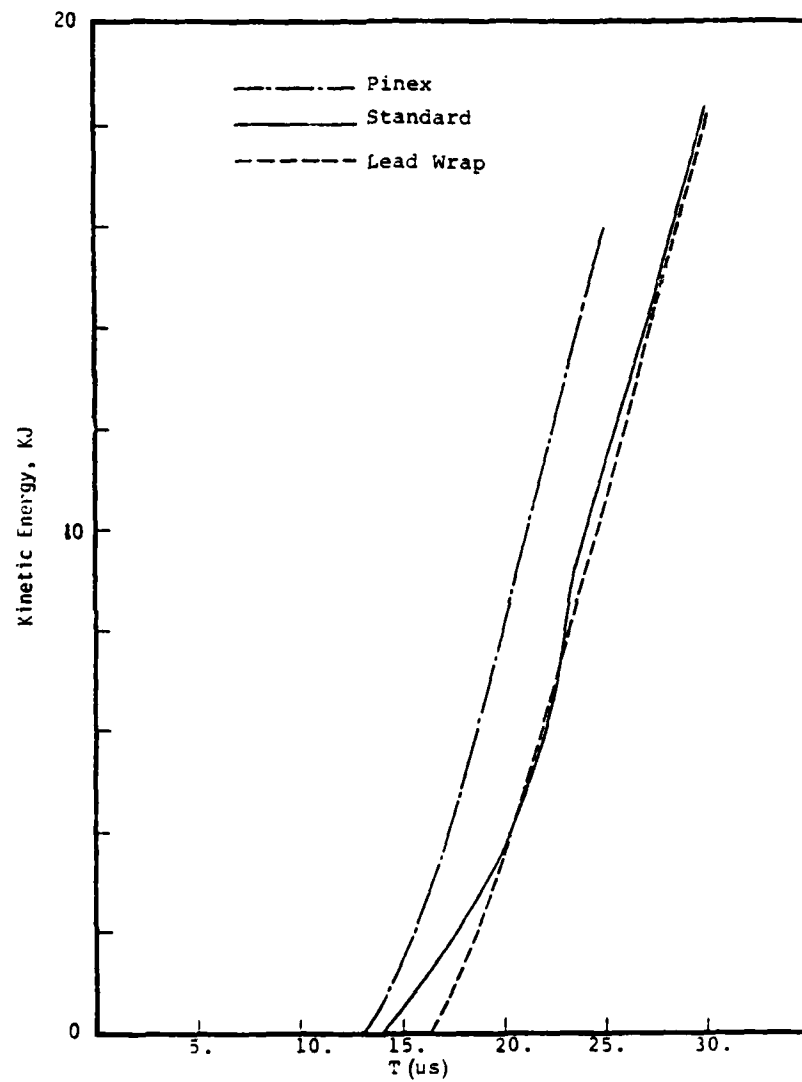


Figure A.4 Flux of condensate kinetic energy out of the computational grid.

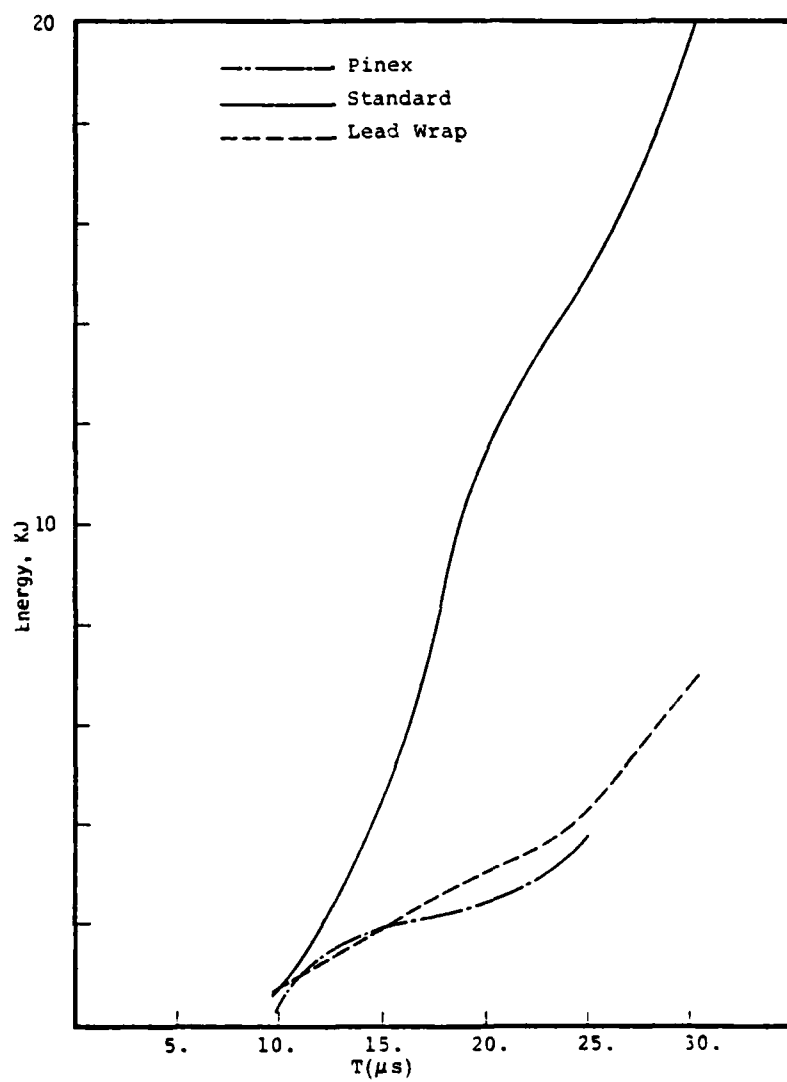


Figure A.5 Flux of total vapor energy out of the computational grid.

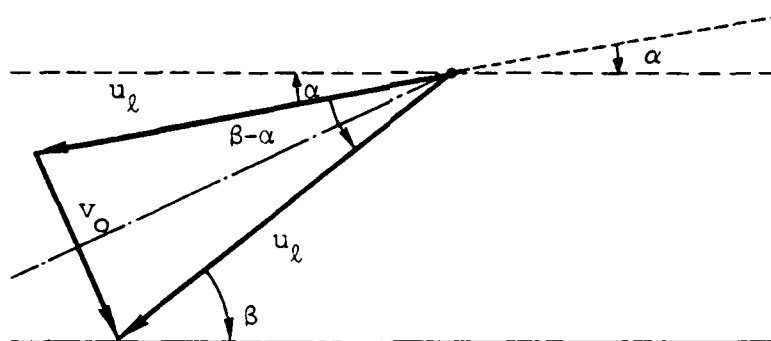
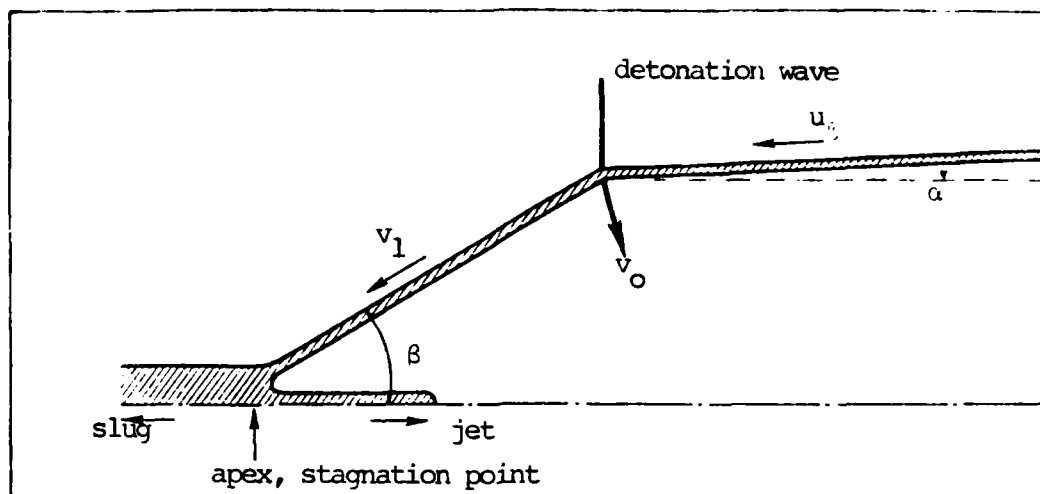


Figure A.6 Impulsive jetting configuration considered in simplified theory.

Since e is changed but little by the impulsive push and $P \approx 0$ on any free surface, all free surface velocities are approximately u_ℓ in the apex frame of reference. This applies to the jet and to the rearward-moving slug. Therefore, in the shock frame, the slug and jet velocities are

$$v_s = -u_\ell \quad (\text{A.5})$$

$$v_j = u_\ell \quad (\text{A.6})$$

In the laboratory frame, $v_s = 0$ and $v_j = 2u_\ell$.

Straightforward application of conservation of mass and axial momentum^(10,11) gives the following:

$$m_j = m \sin^2 \frac{\theta}{2} \quad (\text{A.7})$$

$$m_s = m \cos^2 \frac{\theta}{2} \quad (\text{A.8})$$

where m is the liner mass per unit axial length and m_j , m_s are the components of m entering the jet and the slug. The energy fed into the jet, per unit axial length of pipe, is:

$$\epsilon_j = m_j \frac{v_j^2}{2} = m \frac{v_0^2}{8} \quad (\text{A.9})$$

($m v_0^2/2$ in the laboratory frame).

The above results for impulsively-driven liner jetting may be adapted to the steady shock-driven liner problem. This is different in that the pressure field responsible for collapse remains substantial well behind the shock and the liner continues to accelerate until it reaches the axis (Fig. A.7). The collapsing liner is not conical.

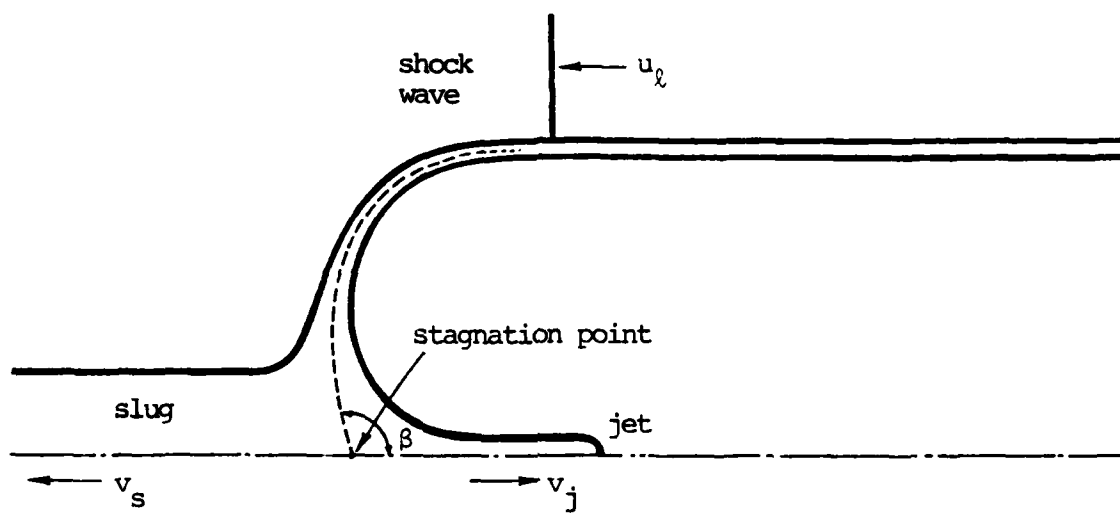


Figure A.7 Steady shock-driven jetting configuration.

It is useful to define β as the total angle turned by the streamline into the stagnation point (Fig. A.7). The stagnation point, which is stationary in the moving frame of reference, now plays the role of the apex. The Bernoulli Equation still holds for the liner. We again obtain the result that all free surface velocities have the magnitude u_ℓ . (Actually, there is substantial pressure in the pipe, but after a steady jet is established this pressure is fairly uniform between the jet and the shock position, and changes of e have been found to be unimportant, so the result still holds.) Eq. A.1 still holds if \vec{v}_0 is the total velocity change imparted by the post-shock pressure field and if the angle of the stagnation streamline does not change much in the region around the stagnation point where pressure changes are appreciable. It follows that the entire set of Eqs. A.1 - A.9 holds.

Equation (A.9) is helpful in understanding the result of nearly-equal \dot{E}_j 's for the various configurations. It states that the jet-ting energy is equal to the kinetic energy of collapse imparted by the driving forces. In the steady shock case this should be proportional to the driving pressure times the collapse distance, $P_s r_0$, which is the same in all calculated configurations.

Now the results of nearly-equal \dot{M}_j 's can be understood. From Eqs. A.6 and A.9:

$$\epsilon_j = \frac{m_j u_\ell^2}{2}$$

$$\text{or } \dot{M}_j = m_j u_\ell = \frac{2\epsilon_j}{u_\ell} = \frac{2\dot{E}_j}{u_\ell^2} \quad (\text{A.10})$$

Since the \dot{E}_j 's and u_ℓ 's are the same for all, so must be the \dot{M}_j 's.

Now the simple theory can be compared with the calculational results. Typical results from each calculation after a quasi-steady flow has evolved are shown in Figs. A.8 and A.19. It should first be pointed out that in the calculations the wet sand stemming and the liner were, for simplicity, fed into the grid at the same velocity $u_\ell = u' = 3.555 \text{ km/sec}$, the velocity of the shocked sand in the shock frame of reference. This would not occur in a real configuration.

First we verify that the solutions satisfy Eq. A.6. The velocity vector plots for the three basic calculations are shown in Figs. A.11, A.15 and A.19. On each of these is shown an arrow corresponding to an axial velocity u_ℓ . Eq. A.6, in the moving frame of reference, requires that $v_j = u_\ell$. It is evident that the flow in the region of the jetting liner most obvious in the tracer plots (location given in Figs. A.8, A.12, and A.16) satisfies this relationship to reasonable accuracy.

It is not possible with the simplified theory to make an a priori prediction of the rates of mass and energy flow associated with jetting. There is not sufficient information to determine β . However, various checks on the internal consistency of the theory can be made. The rates of mass and energy jetting compared with the theory will be the totals for the vapor plus the particulate jet; the theory considers a single jet velocity with no vapor, whereas the calculation allows different velocities for the vapor and the condensed phase. First, values of β will be inferred from calculated values of \dot{M}_j and compared with values estimated from the tracer and contour plots. Table A.1 shows the relevant quantities. Given m and the calculated \dot{M}_j , Eq. A.10 implies a value of m_j and Eq. A.7 implies a value of β . This β is seen to compare reasonably well with values inferred from the tracer plots. The difference is the greatest for the Lead Wrap case, where the thin liner approximation is most suspect. In addition, the asymptotic values of \dot{M}_j estimated from Figs. A.2 and A.3, and especially the values of β estimated from the contour and tracer plots, are only approximate.

Table A.1 Comparison of collapse angles, β° , implied by simplified theory and measured from calculation output

	m(g/cm)	Calculated \dot{M}_j (kg/sec)			m_j (g/cm) $= \dot{M}_j / u_{\ell}$	Inferred β° Eq. A.7	β° Estimated from: Contours/Tracers
		Condensates	Vapor	Total			
Standard	1.413	212	91	303	0.852	102	90
Lead Wrap	16.68	212	37	249	0.700	24	31
Pinex	3.225	212	37	249	0.700	56	58

A value of \dot{E}_j can be inferred from a calculated \dot{M}_j using Eq. A.10. This can be compared with the \dot{E}_j edited from the calculations. The comparisons are shown in Table A.2. The inferred values support the qualitative validity of the simplified theory although they are 25% to 28% low. The effect of partial vaporization of jetted material on jetting efficiency is, of course, not addressed by the theory. It is not unreasonable to expect that this would allow more energy to jet because vapor can escape the stagnation region into the open pipe around the narrow condensate jet. The calculated result is consistent with this expectation.

Table A.2 Comparison of jetting energy rate inferred from \dot{M}_j and calculated directly

	Inferred \dot{E}_j (GJ/sec)	Directly Calculated \dot{E}_j		
		Condensates	Vapor	Total
Standard	1.91	1.59	1.08	2.67
Lead Wrap	1.57	1.59	0.50	2.09
Pinex	1.57	1.59	0.50	2.09

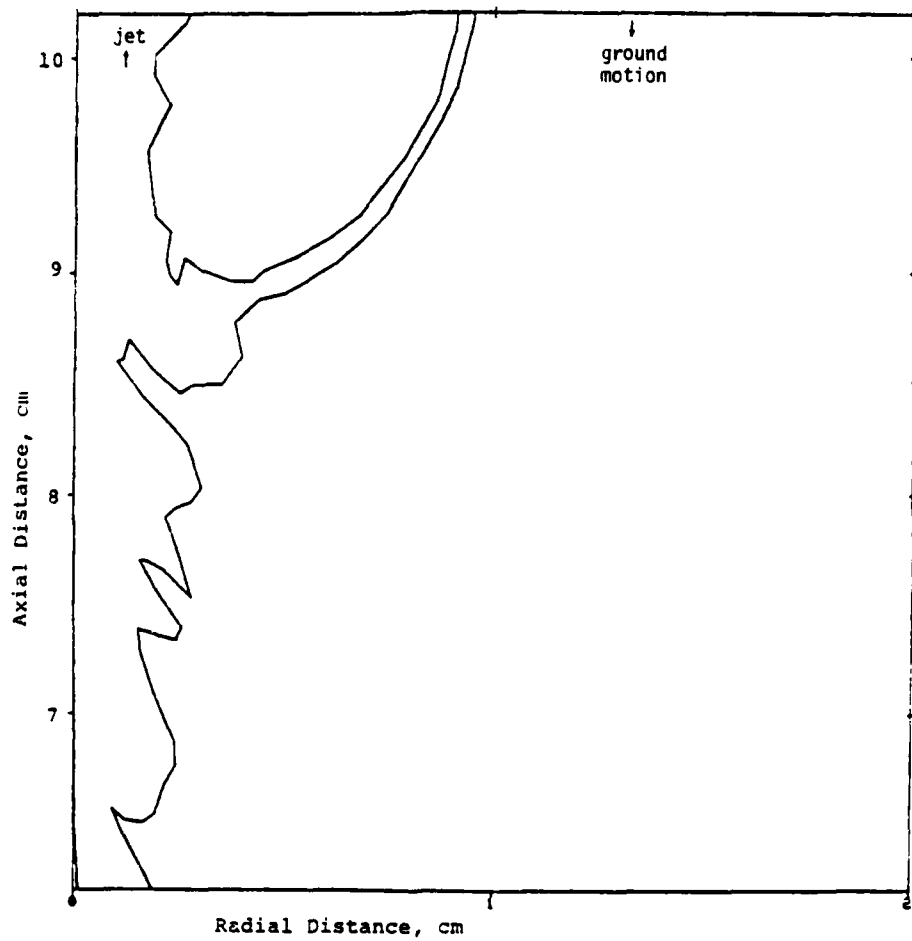


Figure A.8 Tracer positions in idealized Standard configuration, 25 μ s.

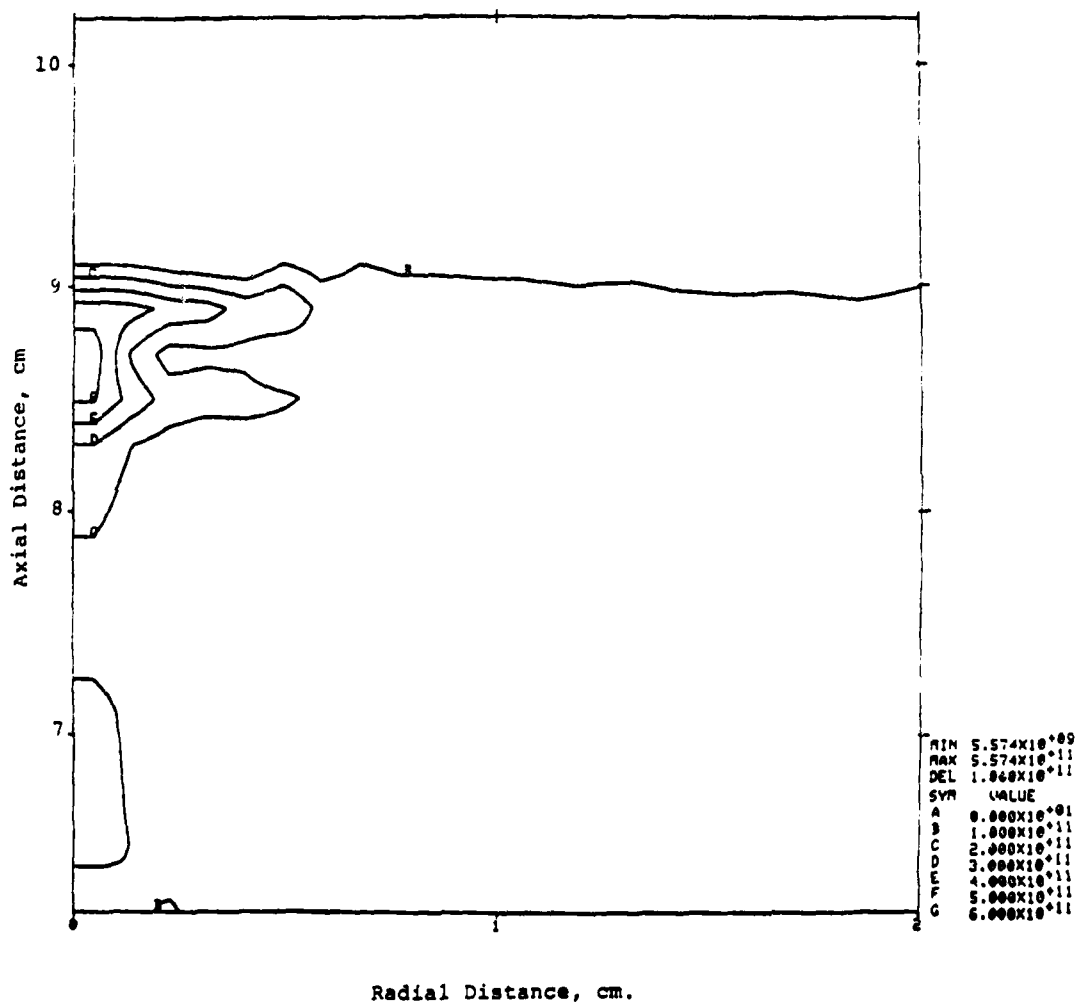


Figure A.9 Pressure contours in idealized Standard configuration, 25 μ s.

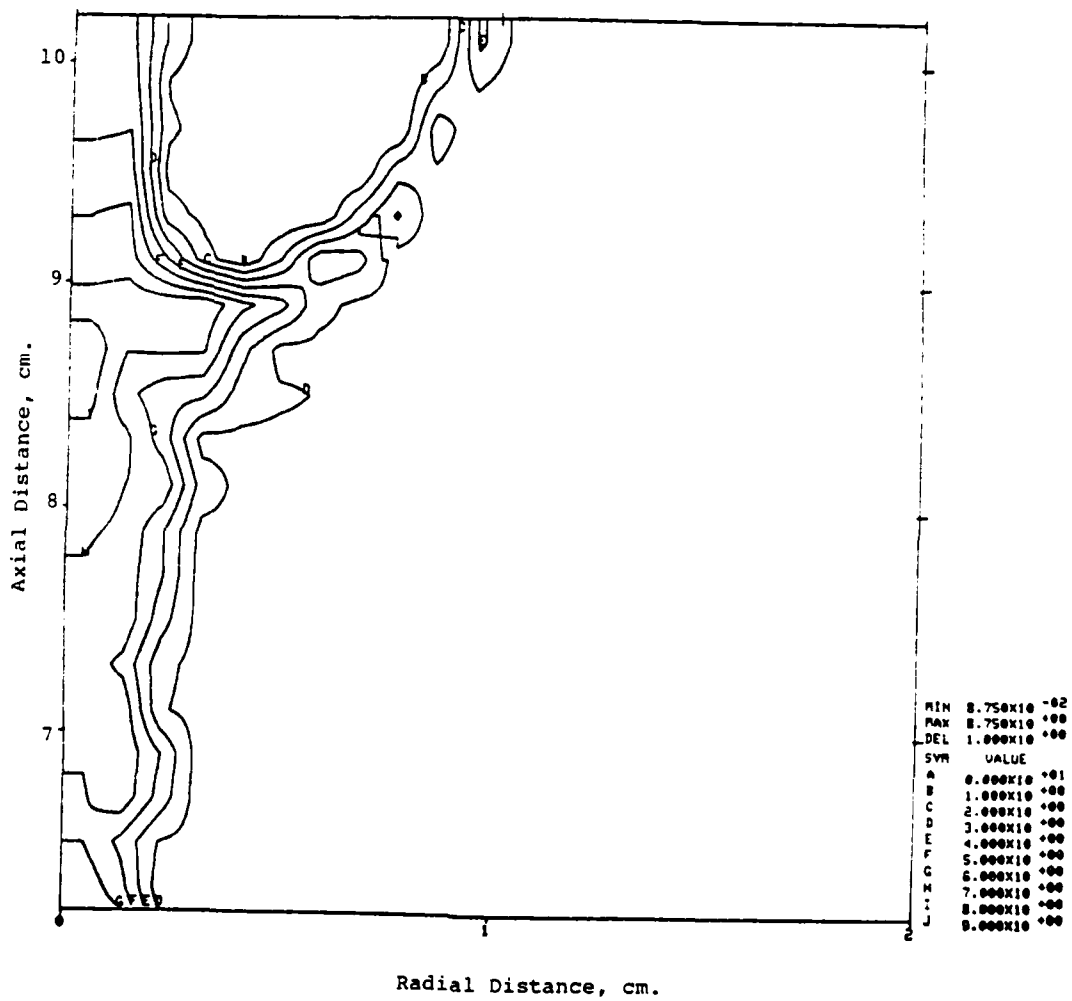


Figure A.10 Density contours in idealized Standard configuration, 25 μ s.

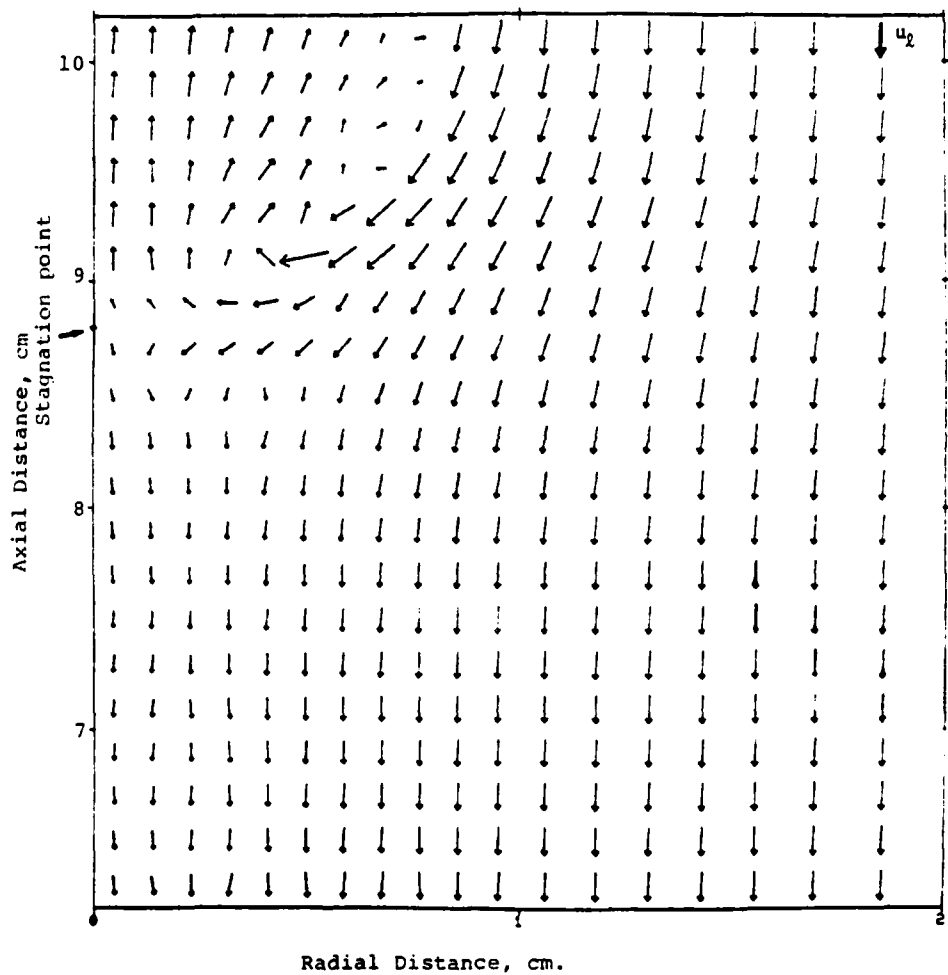


Figure A.11 Velocity vectors in idealized Standard configuration, 25 μ s.

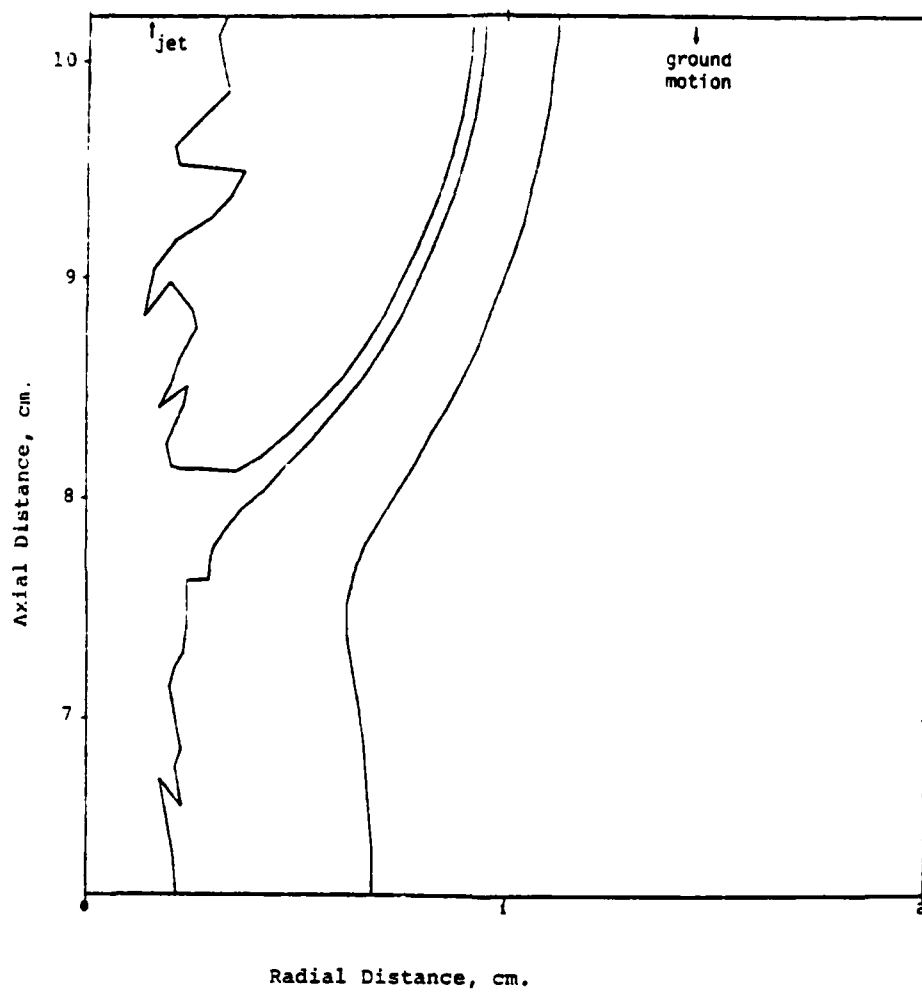


Figure A.12 Tracer positions in idealized Lead Wrap configuration, 25 μ s.

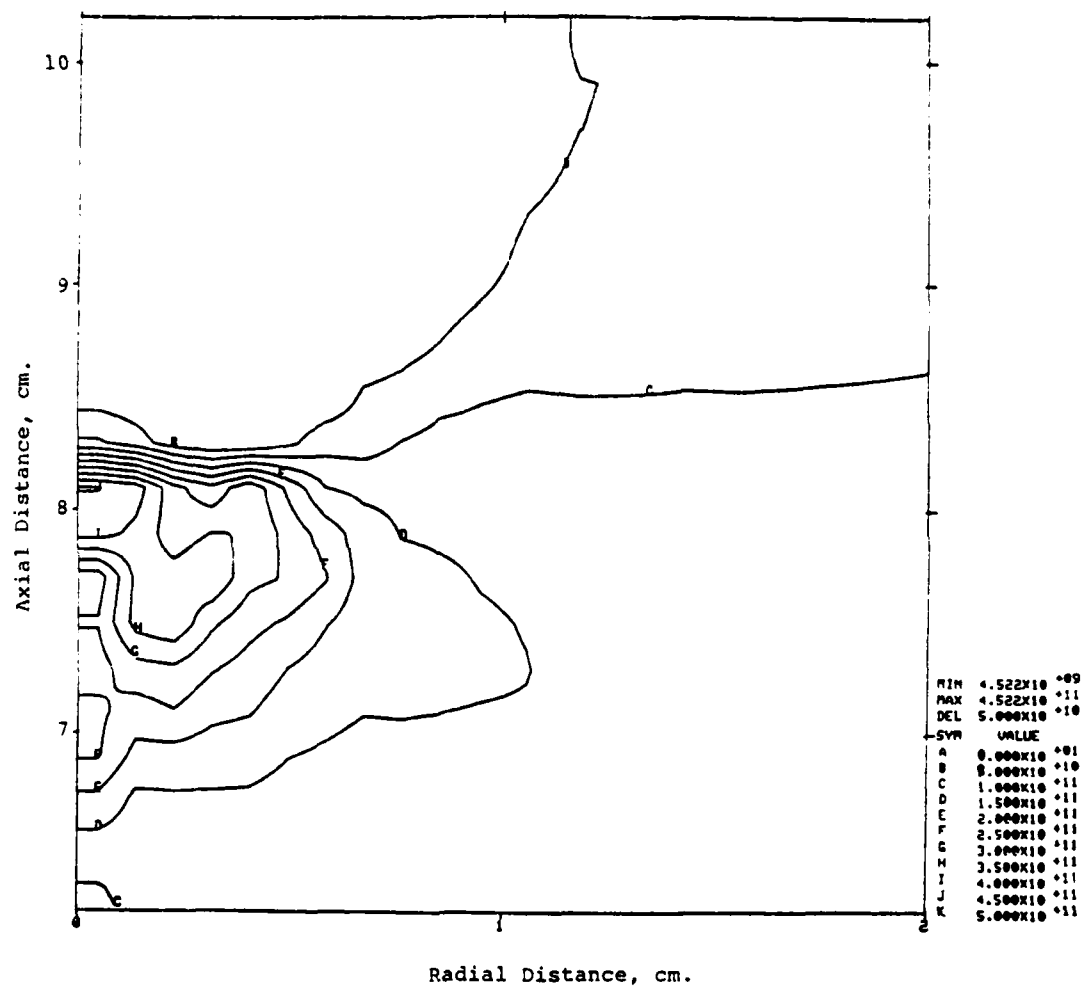


Figure A.13 Pressure contours in idealized Lead Wrap Configuration, 25 μ s.

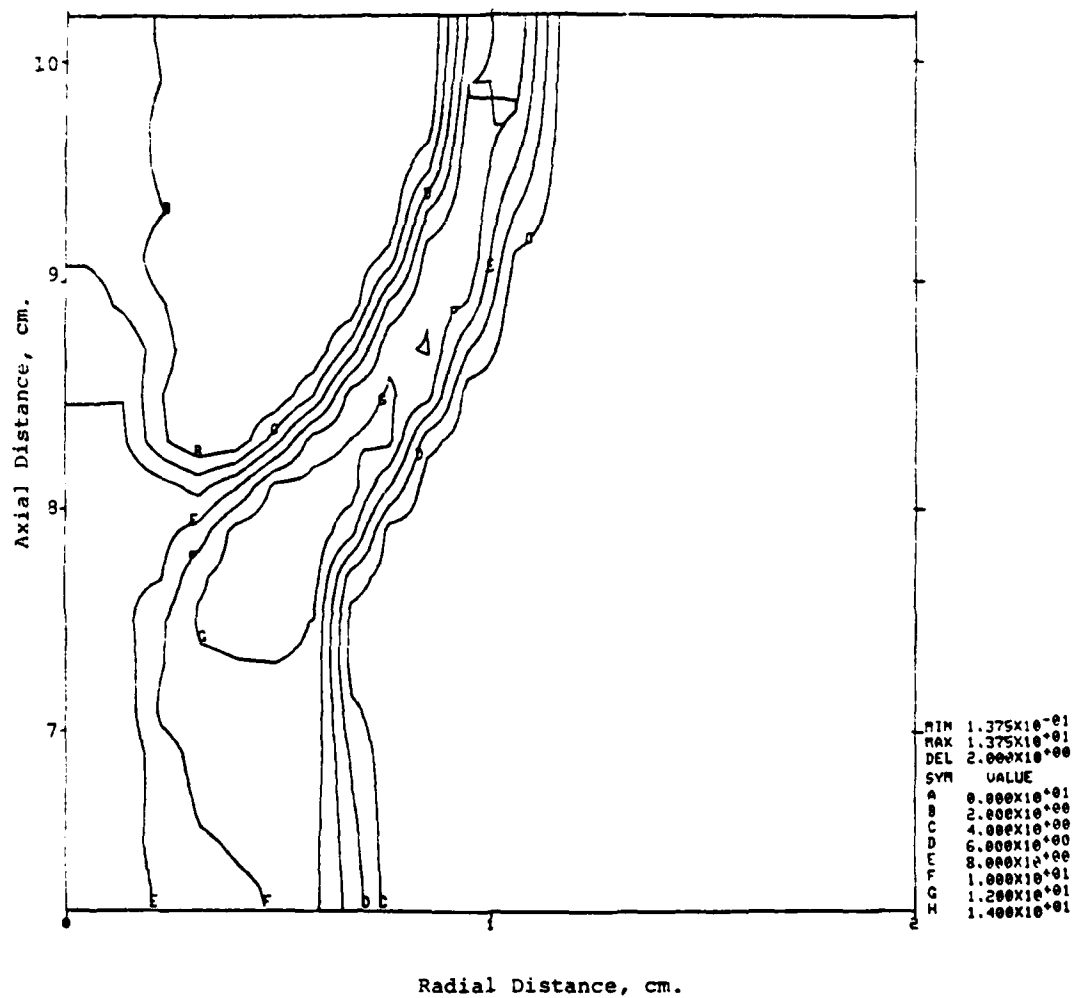


Figure A.14 Density contours in idealized Lead Wrap Configuration, 25 μ s.

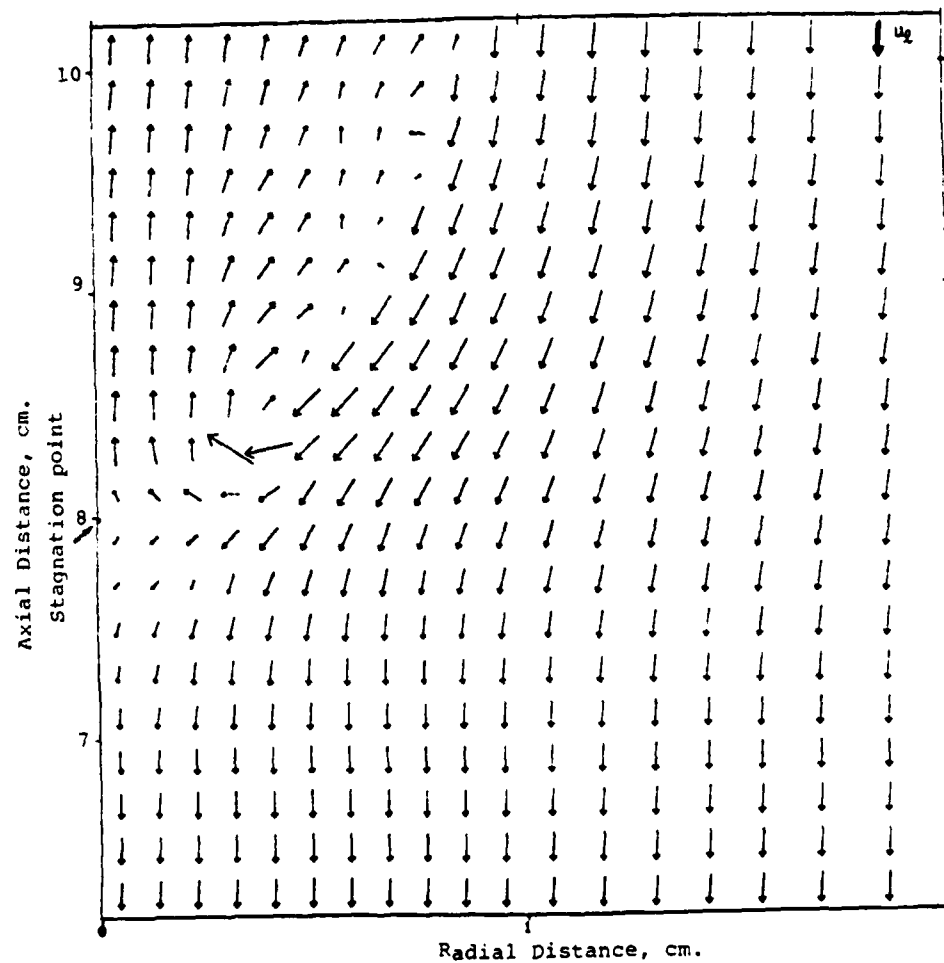


Figure A.15 Velocity vectors in idealized Lead Wrap Configuration, $25 \mu s$.

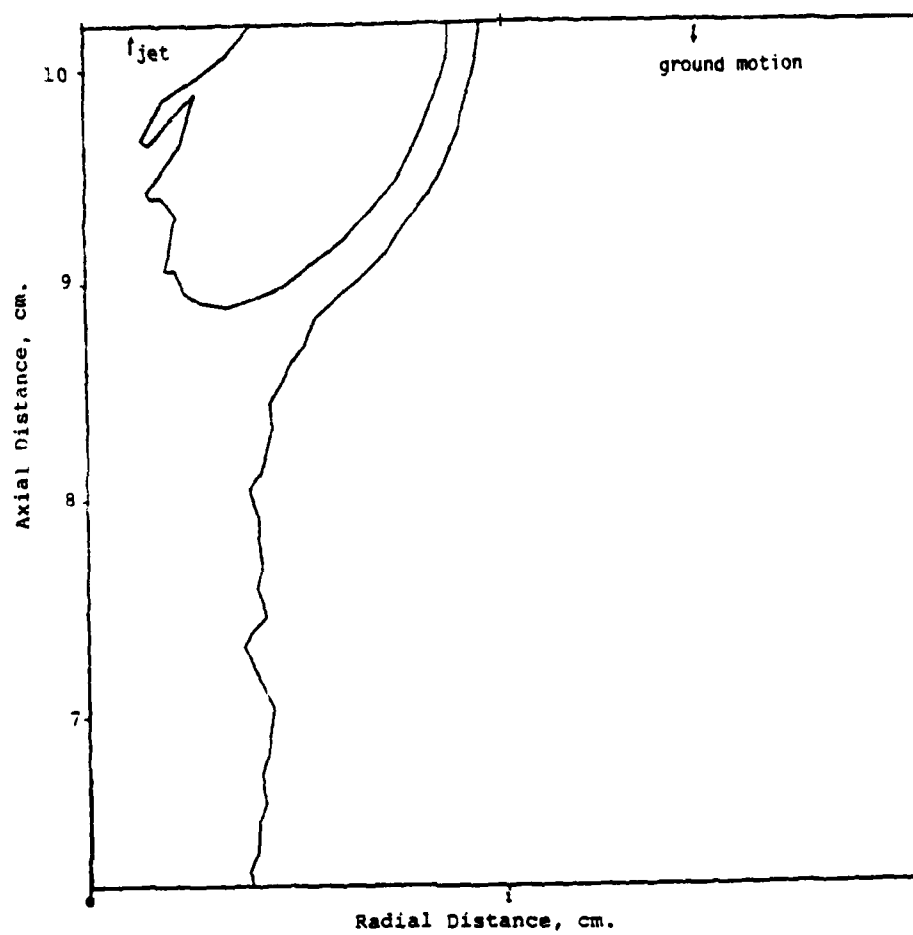


Figure A.16 Tracer positions in idealized Pinex configuration, 25 μ s.

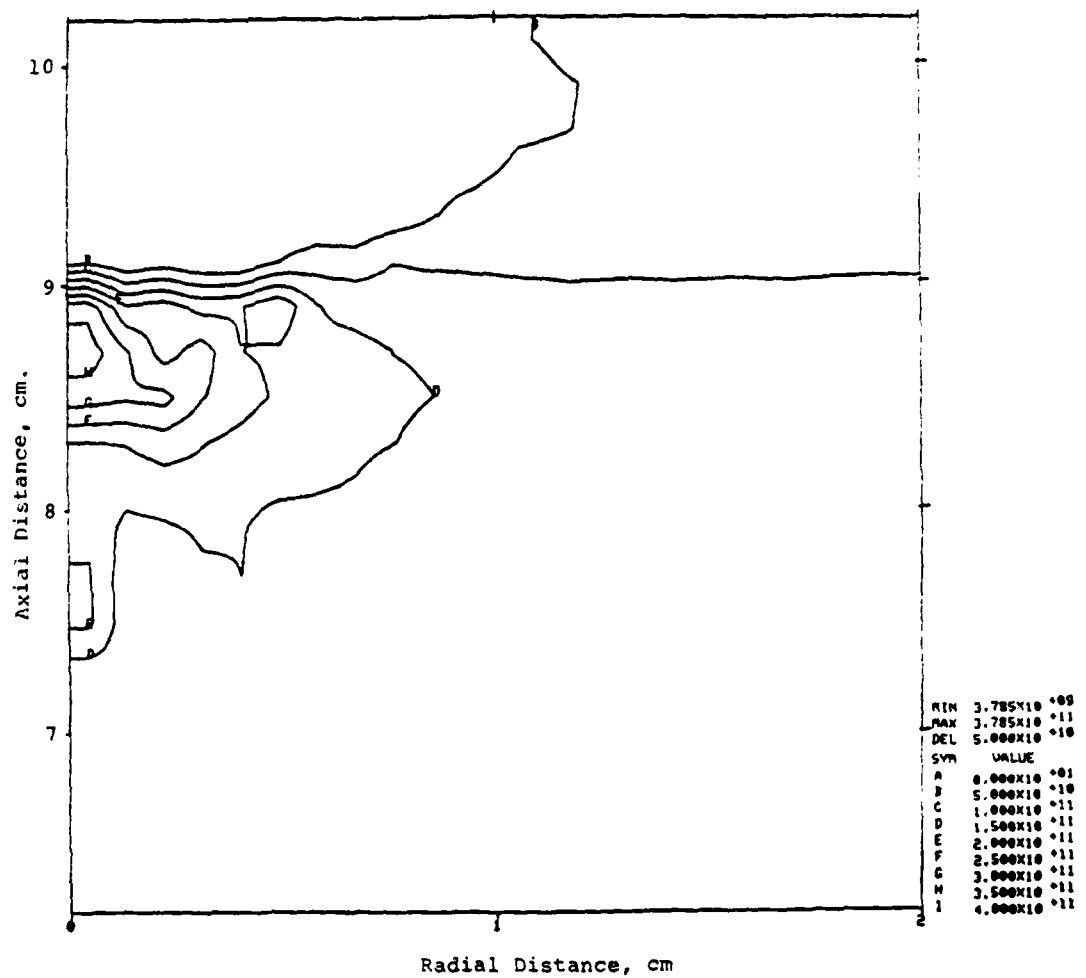


Figure A.17 Pressure contours in idealized Pinex configuration, 25 μ s.

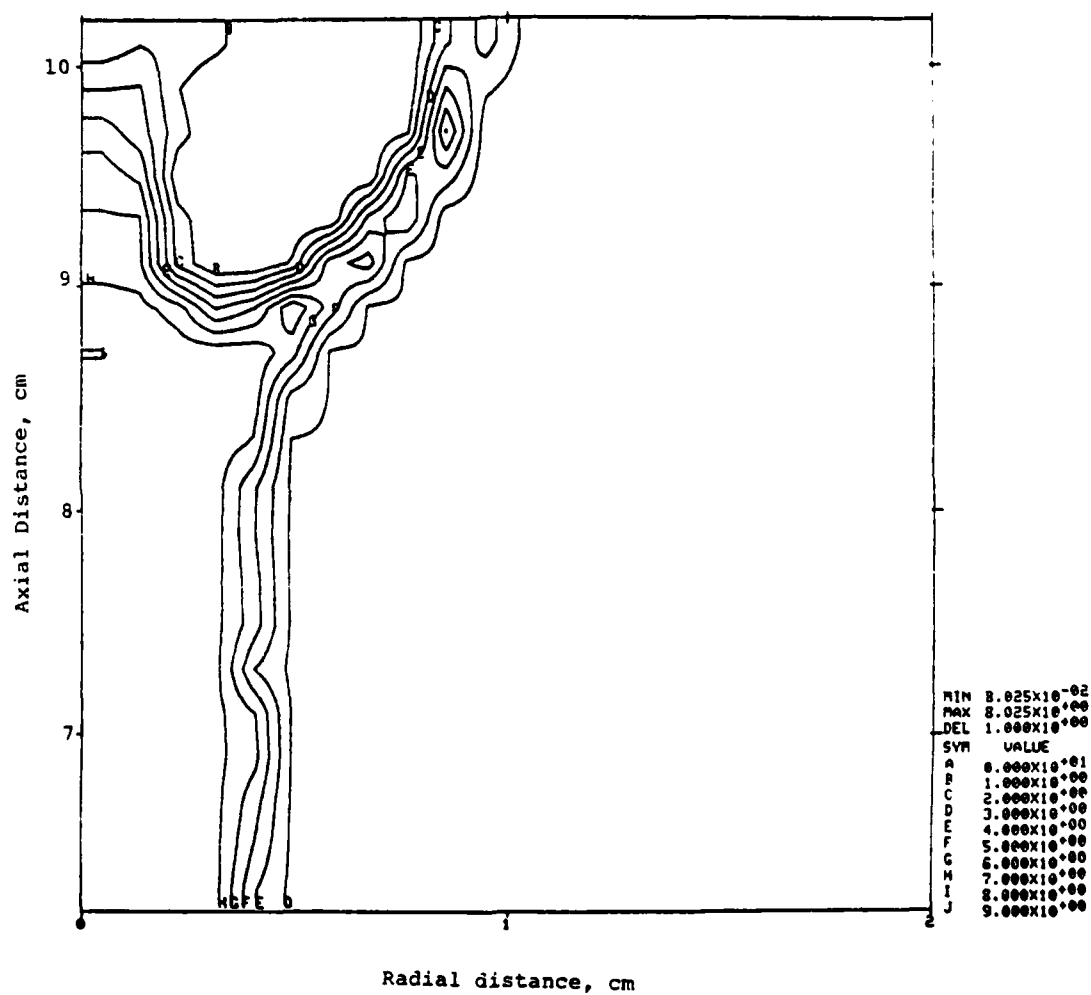


Figure A.18 Density contours in idealized Pinex configuration, 25 μ s.

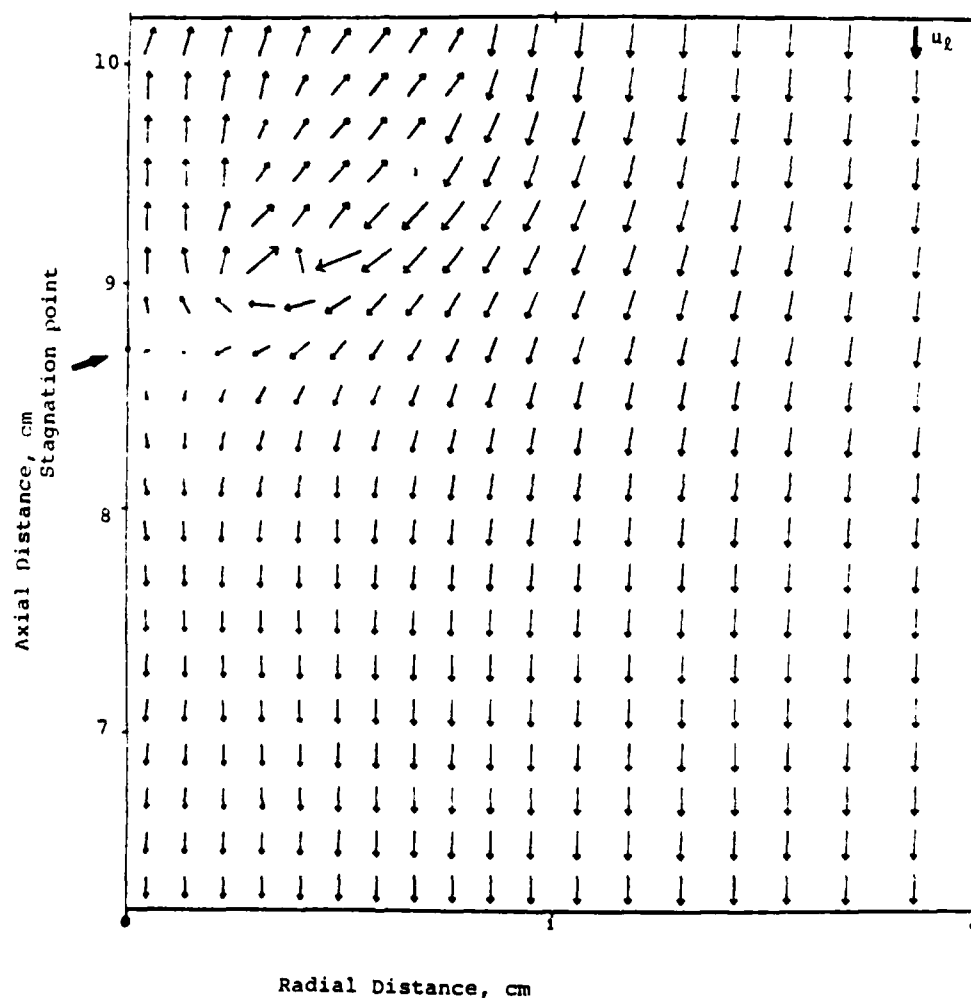


Figure A.19 Velocity vectors in idealized Pinex configuration, 25 μ s.

Eq. A.4 can be used to estimate the pressure at the stagnation point. Ignoring the small pressure and internal energy in the liner as it feeds into the jet, and denoting stagnation conditions with subscript s, the stagnation pressure is approximately

$$P_s \approx \rho_s \left(\frac{u_\lambda^2}{2} - e_s \right) \quad (\text{A.11})$$

The stagnation pressure occurs in the collapsed iron liner. The following simple equation of state for iron may be used:

$$P = A_\mu + B_\mu^2, \quad \mu = \frac{\rho}{\rho_0} - 1 \quad (\text{A.12})$$

where $A = 1.28$ Mbar, $B = 1.05$ Mbar, $\rho_0 = 7.87$ g/cc. e_s , ρ_s , and P_s can be found by a trial and error method satisfying Eqs. A.11, A.12, and $e_s = \int P d(1/\rho)$ assuming an adiabatic compression to the stagnation state. For $u_\lambda = 3.555$ km/sec the result is $P_s = 588$ kbar. The calculations all produce results fluctuating between about 350 and 700 kbar, which is typical of solutions with Eulerian codes at a point of convergence on axis. The agreement between the calculations and the estimate with Eqs. A.11, A.12 is considered good.

It is concluded that the simple theory is quite consistent with the calculational results, despite its simplicity. In particular, it does not consider the effect of partial vaporization of the liner, and it assumes a thin liner. The latter assumption is highly questionable in the Lead Wrap case. This is also the case where the inferred and calculated β 's are in greatest disagreement (about 25%). It is important to emphasize that only qualitative comparisons with simple theory are possible because the asymptotic values of the calculated \dot{M}_j and \dot{E}_j are known only approximately and there is considerable uncertainty

in the value of β° estimated with the aid of tracer and contour plots - especially in the Lead Wrap case. The former difficulty can be reduced by running the calculations longer; the latter cannot.

It is also concluded that the zoning employed in these steady shock frame calculations is adequate for the calculation of jetting with a spherically diverging shock.

APPENDIX B

AERODYNAMIC TWISTING OF THE HELICAL SPIRAL

The stagnation of the flow against the forward face of the spiral generates a torque about the point "O" in Figure B.1. This causes an angular displacement, θ . As θ increases, the torque increases rapidly and so does the angular acceleration, $\ddot{\theta}$.

The following analysis provides an estimate of the characteristic time required for θ to become very large. Rigid body rotation about the point O is assumed. This tends to underestimate the rate of turning because the spiral seems likely to bend about some intermediate point along the length L and, therefore, to have in effect a smaller moment of inertia. On the other hand, the omission of strength effects tends to overestimate the turning rate. We feel that, on balance, the estimate is pessimistic (an underestimate) because the strength effect is small; this will be justified later. Slippage of the point O downstream along the wall is also likely to occur but this should not change the conclusions.

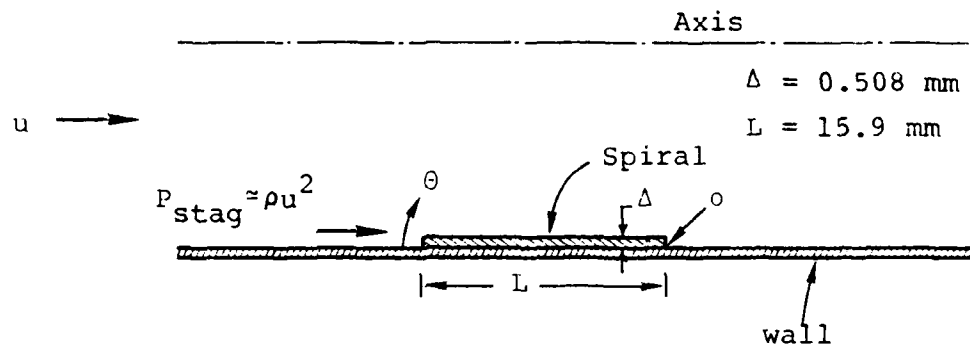
The moment of inertia (I) and the torque (T) per unit depth into the diagram of Figure B.1 may be expressed as follows:

$$I = \frac{\rho_H \Delta L^3}{3} \quad (B.1)$$

$$T = \frac{\rho u^2}{2} [L \sin \theta + \Delta \cos \theta]^2 \quad (B.2)$$

The angular acceleration is

$$\ddot{\theta} = T/I \quad (B.3)$$



(a) Initial configuration



(b) After start of twisting

Figure B.1 Geometry of twisting spiral.

Since this analysis has only qualitative validity, it is justifiable to simplify the problem by linearizing in θ . This will give a readily integrable equation for $\theta(t)$ which is valid for small θ . The solution diverges at time t_∞ ; t_∞ will be taken as an estimate of the characteristic time for θ to become "large".

$$\ddot{\theta} = \frac{3}{2} \frac{\rho u^2}{\rho_H \Delta L} [L \theta + \Delta]^2 \quad (B.4)$$

For convenience, let

$$a = \frac{3}{2} \frac{\rho u^2}{\rho_H \Delta L}, \quad b = \frac{\Delta}{L}.$$

Then

$$\ddot{\theta} = a(\theta + b)^2$$

With the substitutions

$$\phi = \theta + b, \quad \tau = \sqrt{a} t :$$

$$\phi'' = \phi^2$$

The initial conditions are

$$\phi'(0) = 0, \quad \phi(0) = b.$$

The initial condition on ϕ' will be satisfied only approximately.

Two solutions are available:

$$\phi = \frac{A}{(B \pm \tau)^2}, \quad \phi' = \mp \frac{2A}{(B \pm \tau)^3}, \quad \phi'' = \frac{6A}{(B \pm \tau)^4},$$

where A and B are constants. The difficulty is that these cannot be superposed to satisfy the initial conditions. The differential

equation requires that $A = 6$. Assuming $B \geq 0$, the lower sign must be used so that $\phi' \geq 0$ as required physically. $\phi'(0) > 0$, in contradiction to the requirement, but it is sufficiently small to be acceptable (this will be verified later). From the other initial condition,

$$\phi(0) = b = \frac{A}{B^2} = \frac{6}{B^2}$$

It follows that

$$B = (6L/\Delta)^{1/2},$$

$$\phi'(0) = \left(\frac{2}{3}\right)^{1/2} \left(\frac{\Delta}{L}\right)^{3/2}$$

$$\dot{\theta}(0) = \left(\frac{\rho}{\rho_H}\right)^{1/2} \frac{u\Delta}{L^2} \quad (B.5)$$

$$\theta = \frac{\Delta/L}{(1 - t/t_\infty)^2} - \Delta/L \quad (B.6)$$

where

$$t_\infty = \frac{2L}{u} \left(\frac{\rho_H}{\rho}\right)^{1/2} \quad (B.7)$$

$\theta \rightarrow \infty$ as $t \rightarrow t_\infty$.

Equations (B.5) and (B.7) yield the following

$$\dot{\theta}(0)t_\infty = 2\Delta/L$$

i.e., if the unwanted initial angular velocity $\dot{\theta}(0)$ inherent in the above solution were sustained for the time t_∞ the angular displacement would only be $2\Delta/L$. This has no significant effect on the analysis.

The solution for $\theta(t)$ has the intuitively expected characteristic of slow early growth with an eventual rapid buildup of acceleration. For the example in Fig B.1, $\Delta/L = 0.032$, the following values are obtained:

t/t_∞	$\theta(\text{radians})$
0.127	0.01
0.293	0.032
0.508	0.1
0.824	1.0

For $L = 15.9\text{mm}$ and $\rho u^2 = 10\text{ kbars}$, typical of conditions nearer the source, $t_\infty = 89\text{ }\mu\text{s}$ for a steel helix ($\rho_H = 7.8$) and $t_\infty = 32\text{ }\mu\text{s}$ for $\rho_H = 1$ (a plastic). This may explain why the steel helix in the first 300 mm (LS IV-22) was less effective than the polyolefin helix in the first 229 mm (LS III-16).

For conditions near the witness plate $\rho u^2 = 3\text{ kbars}$ is more typical, according to both calculations and data. The plasma leads the particulates by about $60\text{ }\mu\text{s}$. t_∞ is only $58\text{ }\mu\text{s}$ for $\rho_H = 1$, therefore, a polyolefin spiral should effectively occlude the pipe. For $\rho_H = 7.8$, $t_\infty = 162\text{ }\mu\text{s}$. In $60\text{ }\mu\text{s}$ a steel helix with $\Delta/L = 0.032$ will turn only 2.8° , allowing the edge to protrude only about 1.3 mm into the stream (including the 0.5 mm spiral thickness). Although the 3.2 mm lead baffle (LS II-5, III-12, and IV-10, 11) was sufficient to stop the particulates, the baffle may have been displaced or rotated into the stream; hence, a 1.3 mm protrusion of spiral may be marginal or worse.

Another phenomenon, not yet considered, may greatly increase the protrusion of the helix. A twist imparted locally will propagate downstream along the helix, giving it an initial displacement, a head start. If the head start is only $\theta = \Delta/L$, a time $t = 0.29 t_\infty$ can be saved. This would suggest that after exposure to 3 kbar for $60\text{ }\mu\text{s}$ in

the above example a steel helix might be turned at an angle appropriate for $t/t_{\infty} = (60/162) + 0.29$ or 0.66, i.e., 14° , and protrude about 4 mm into the stream. The propagation of twist may play a significant role in the success of the helix. If this is so, the use of thin rings would not be as effective, especially if the material is steel.

It remains to justify the neglect of the strength of the helix material. The sketch in Fig. B.2 is helpful in visualizing the effect. The helix is viewed as uncoiled into a straight strip but experiencing a twist about the centerline of that configuration. The twist considered is only that which results from the difference between aerodynamically-induced rotations at different axial locations. The question is whether the torsion resulting from this twist will significantly reduce the rotation. The twist inherent in the forming of the helix is ignored. Bending of the helix in the plane of Fig. B.1 is not considered; if it occurs, it only enhances the intrusion of the helix into the pipe.

As the spiral material twists, it develops internal torsional stress which resists further twisting. The torsional moment about the centerline is

$$\tau = \frac{\beta}{\ell} \frac{E_s A^4}{4\pi^2 J}$$

where E_s = shear modulus ≈ 80 kbars for steel; J = polar moment of inertia of the cross section about the centerline $= \Delta L^3/12$; A = cross sectional area, L_Δ . Therefore,

$$\tau = \frac{\beta}{\ell} \frac{3}{\pi} \Delta^3 L E_s \quad (B.8)$$

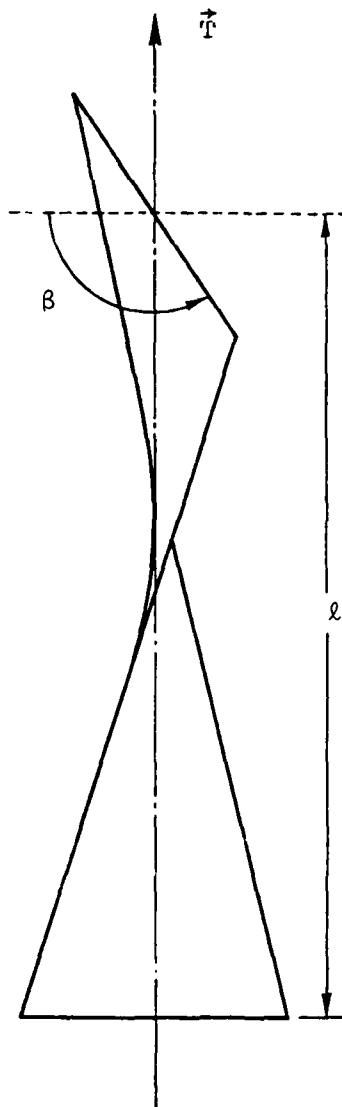


Figure B.2 Resistance of the helical sheet to twisting.

Consider only the influence of the torsion resulting from the aerodynamic twisting: β is, then, the difference in θ over a length along the spiral. A generous value of β/ℓ is that which corresponds to a full right angle twist in one loop around the pipe:

$$\beta/\ell = \cos \alpha / 4R \quad (B.9)$$

where α = pitch angle and R = pipe radius.

The ratio of the aerodynamic torque per unit length to the torsional moment per unit length is, from Eqs. (B.2), (B.8), and (B.9):

$$\frac{T_a}{T_m} \approx \left(\frac{4\pi^3}{3}\right) \left(\frac{\rho u^2}{E_s}\right) \left(\frac{LR^2}{\Delta^3}\right) \left(\frac{\sin \theta + \frac{\Delta}{L} \cos \theta}{\cos \alpha}\right)^2$$

Taking $\rho u^2 = 10$ kbar, $\alpha = 40^\circ$, and the values of Δ , L , and R from the PI simulations,

$$\frac{T_a}{T_m} \approx \begin{cases} 10^5 & \text{for } \theta = \pi/2 \\ 10^2 & \text{for } \theta = 0 \end{cases}$$

The higher value is much more relevant to the situation posed. In either case, however, the resistance of even a steel spiral to twisting appears to be small compared to the applied aerodynamic moment, and the approximations made in the dynamic analysis appear justified.

DISTRIBUTION LIST

DEPARTMENT OF DEFENSE

Defense Nuclear Agency

ATTN: SPTD, T. Kennedy
4 cy ATTN: TITL

Defense Technical Information Center

12 cy ATTN: DD

Field Command

Defense Nuclear Agency

ATTN: FCTT, W. Summa
ATTN: FCTT, G. Ganong
ATTN: FCT, P. Oppedahl
3 cy ATTN: FCTK, B. Ristvet
3 cy ATTN: FCTK, C. Keller

Field Command Test Directorate

Test Construction Division

Defense Nuclear Agency

ATTN: FCTC, J. Lacombe

DEPARTMENT OF ENERGY

Department of Energy

Nevada Operations Office

ATTN: R. Newman

Desert Research Institute

ATTN: D. Schulke Sec Off for C. Case
ATTN: D. Schulke Sec Off for P. Fenske

OTHER GOVERNMENT AGENCY

Department of the Interior

U.S. Geological Survey

ATTN: R. Carroll
ATTN: A. Fernald

DEPARTMENT OF ENERGY CONTRACTORS

Lawrence Livermore National Lab

ATTN: B. Hudson
ATTN: J. Shearer
ATTN: L-209, G. Higgins
ATTN: R. Terhune
ATTN: L. Makague

DEPARTMENT OF ENERGY CONTRACTORS (Continued)

Los Alamos National Laboratory

ATTN: J. Wing
ATTN: E. Jones
ATTN: R. Brownlee
ATTN: F. App
ATTN: T. Kunkle
ATTN: B. Travis

Sandia National Lab

ATTN: C. Mehl
ATTN: C. Smith

DEPARTMENT OF DEFENSE CONTRACTORS

California Research & Technology, Inc

ATTN: M. Rosenblatt

Kaman Tempo

ATTN: DASIAC

Pacific-Sierra Research Corp

ATTN: H. Brode

Pacifica Technology

ATTN: D. Patch

Physics International Co

ATTN: D. Munna
ATTN: E. Moore

R & D Associates

ATTN: P. Haas

SRI International

ATTN: A. Florence

Systems, Science & Software, Inc

ATTN: C. Dismukes
ATTN: R. Duff
4 cy ATTN: J. Bartchel
4 cy ATTN: J. Wiehe

FILMED

22-8